Macroscopic orientation of inertial flows in porous media

Yanis Bendali, Morgan Chabanon, Quentin Holka, Benoît Goyeau

Macroscopic orientation of inertial flows in porous media

Yanis Bendali[1,2], Morgan Chabanon[1,*], Quentin Holka[2], and Benoît Goyeau[1,*]

[1]Université Paris-Saclay, CNRS, CentraleSupélec, Laboratoire EM2C, Gif-sur-Yvette 91190, France
[2]Safran Tech, Magny-Les-Hameaux 78114, France
[*]Co-corresponding authors: morgan.chabanon@centralesupelec.fr; benoit.goyeau@centralesupelec.fr

Keywords: porous media; inertial flow; Forchheimer; flow orientation; up-scaling; volume averaging method; closure; linearization

Abstract

Macroscopic models of inertial flows in porous media have many practical applications where direct numerical simulations are not feasible. The Forchheimer equation describes macroscopic momentum transport accounting for inertial effects at the pore scale through a non-linear correction tensor $\mathbf{F}_\beta$. Using up-scaling approaches such as the volume averaging method, $\mathbf{F}_\beta$ can be determined through the resolution of a closure problem. However this later is non-linear and still depends on the intensity and orientation of the macroscopic flow, complicating its resolution. Moreover, while the influence of the pore Reynolds number on the Forchheimer correction has been studied in details, its dependency on the flow orientation has drawn much less attention. In this work, a system of linearized closure problem is proposed and solved, allowing to determine $\mathbf{F}_\beta$ without the need to solve the full closure problems for each orientation of the macroscopic pressure gradient. The validity of this approach is assessed for various rectangular unit cells against numerical solutions of the corresponding non-linear problem, showing excellent agreement for pore Reynolds number up to unity. Then macroscopic simulations are performed to evaluate the importance of varying flow orientation on the macroscopic inertial flow. Numerical results of the general non-linear macroscopic model obtained by the volume averaging method highlight the necessity to account for extra-diagonal terms as well as macroscopic gradient orientation in the determination of the Forchheimer tensor.

1 Introduction

Inertial laminar flows in porous media are present in a wide range of environmental or industrial systems such as atmospheric flows in canopies [38, 46], geological flows [3, 14], and heat exchangers [4, 29, 32]. Although direct numerical simulation (DNS) of such flows can be performed at the pore scale, the complexity of the local geometry as well as the length scale separation between the pore and the macroscopic system require prohibitively massive computing resources for most applications.

This has motivated the use of macroscopic models of transport phenomena in porous media, where macroscopic conservation equations and effective parameters can be obtained by averaging

the local (pore-scale) equations. For incompressible non-inertial flows, averaging Stokes equation results in Darcy's law where the filtration velocity is linearly dependent on the pressure gradient through the intrinsic permeability tensor $\mathbf{K}_\beta^*$ [15, 19, 55]. This linearity holds for pore Reynolds number up to one [54]. Above this value, it is the Navier-Stokes equation that must be homogenized, resulting in a macroscopic equation analogous to Darcy's law but with an additional non-linear term called the Forchheimer tensor $\mathbf{F}_\beta^*$ that accounts for inertial effects [19, 56]. In this case, the macroscopic equation that relates the seepage velocity $\langle \mathbf{v}_\beta^* \rangle$ to the macroscopic pressure gradient $\nabla \langle p_\beta^* \rangle^\beta$ is known as the Forchheimer equation, and can be written in the absence of gravity as

$$\langle \mathbf{v}_\beta^* \rangle = -\frac{\mathbf{K}_\beta^*}{\mu_\beta} \cdot \nabla \langle p_\beta^* \rangle^\beta - \mathbf{F}_\beta \cdot \langle \mathbf{v}_\beta^* \rangle = -\frac{\mathbf{H}_\beta^*}{\mu_\beta} \cdot \nabla \langle p_\beta^* \rangle^\beta \tag{1}$$

where $\mathbf{H}_\beta^* = \left(\mathbf{I} + \mathbf{F}_\beta^* \right)^{-1} \cdot \mathbf{K}_\beta^*$ is the global permeability tensor and μ_β is the dynamic viscosity of the fluid. Here and in the rest of this article, the subscript β designates quantities defined in the fluid phase β, and the * exponent indicates dimensional quantities.

Recent studies identified distinct inertial flow regimes corresponding to the onset of inertia effects on the pore scale flow structure [1, 2, 23, 24, 31, 52]. The dependency of the Forchheimer correction with the Reynolds number have been largely discussed in the literature, as detailed for instance in Lasseux et al. 2019 [25]. Briefly, for pore Reynolds number slightly greater than one, a *weak inertia regime* characterized by a cubic correction of Darcy's law was identified. Then for larger pore Reynolds numbers up to hundred, a *strong inertia regime* showing a quadratic dependency on the pore Reynolds number was found to occur for various geometries of periodic unit cells. Other transition regimes were observed between unsteady laminar and turbulent flows at pore Reynolds number around hundred. In this case, the transient nature of the flow requires a time-averaging procedure that assumes a linear Forchheimer correction [12, 17, 28, 47, 59]. Although this hypothesis is in agreement with experimental observations, its theoretical justification remains unclear.

Forchheimer's equation (Eq. (1)) has been derived by Whitaker using the volume averaging method [56] to formally upscale Navier-Stokes from the pore to the macroscopic scale. Note that the form shown in Eq. (1) neglects additional terms arising from the up-scaling procedure, in particular the viscous diffusion term also known as the Brinkman correction. In addition to the macroscopic transport equation, the volume averaging method provides a series of closure problems which solutions allow to determine the effective transport properties involved in the global permeability tensor. The closure problem associated with the intrinsic permeability is linear while the one associated with the Forchheimer correction is non-linear and still depends on a local velocity field [24–27, 39]. To solve this non-linear problem, it has been proposed to first solve an associated local flow problem on a periodic unit cell for each values of the pore Reynolds number [1, 2, 24, 52] and macroscopic pressure gradient orientation [11, 24, 37, 53]. As a result, the Forchheimer tensor is an implicit function of these two dimensionless parameters.

Although the dependency of the Forchheimer tensor with the pore Reynolds number has been the subject of several studies leading to the classification of weak inertial flow regimes described above [1, 2, 23, 24, 31, 39], the influence of the macroscopic pressure gradient orientation has drawn much less attention. Importantly, extra-diagonal components of the tensor are not null when the macroscopic flow is not aligned with the elementary geometry. This aspect can become essential

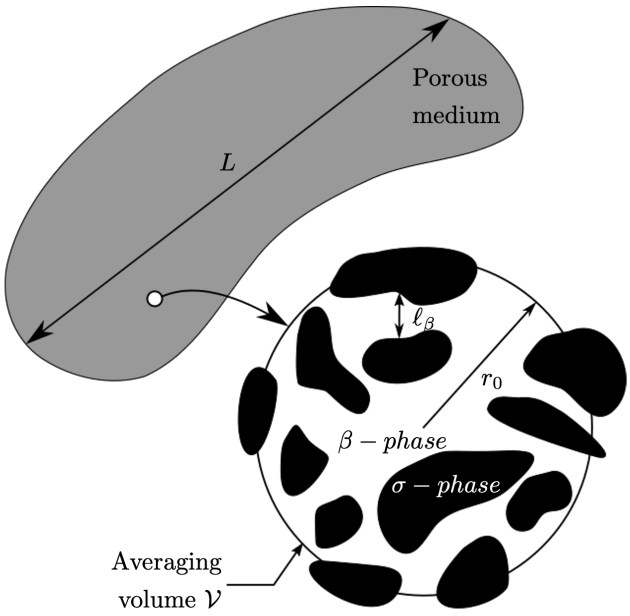

Figure 1: Schematic of a representative elementary volume (REV) with the definitions of the pore-scale phases and length scales.

in cases where the orientation of macroscopic flow varies with respect to the porous arrangement, such as in elbows or curved channels produced by additive manufacturing.

In this work, the effect of the macroscopic flow orientation on the Forchheimer correction tensor is studied in two ways. First, the local inertial flow is up-scaled using the volume averaging method in Section 2. The resulting general closure problem is then linearized in Section 3 by generalizing previous work for arbitrary macroscopic pressure gradient orientation and small pore Reynolds number [7, 31, 39]. The ability to predict the Forchheimer tensor of this linearized model is assessed on rectangular unit cells through comparisons with the classical non-linear model [24, 56] to determine its range of validity in Reynolds number and orientation of the macroscopic pressure gradient. Finally, in Section 4, simulations of macroscopic inertial flow with varying pressure gradient orientation are performed. The prediction of two macroscopic models are assessed against direct numerical simulation. It is shown that, in contrast to diagonal-tensor models often encountered in CFD softwares [11, 37, 53], the non-linear macroscopic model obtained with the volume averaging method is able to correctly capture inertial flow structures and pressure losses in an elbow channel filled with a square porous medium.

2 Up-scaling inertial flow in porous media

At the pore scale, two phases are considered: a Newtonian fluid (β-phase) and an immobile non-permeable solid (σ-phase). The flow is assumed incompressible, laminar and steady. The velocity field $\mathbf{v}_\beta^*$ and pressure p_β^* in the fluid β verify the incompressible Navier-Stokes equations with no-slip boundary conditions at the fluid-solid interface $A_{\beta\sigma}$. The boundary value problem at the pore

scale is therefore

$$\nabla \cdot \mathbf{v}_\beta^* = 0 \quad \text{in} \quad V_\beta \tag{2a}$$

$$\rho_\beta \mathbf{v}_\beta^* \cdot \nabla \mathbf{v}_\beta^* = -\nabla p_\beta^* + \mu_\beta \nabla^2 \mathbf{v}_\beta^* \quad \text{in} \quad V_\beta \tag{2b}$$

$$\mathbf{v}_\beta^* = 0 \quad \text{at} \quad A_{\beta\sigma} \tag{2c}$$

Here ρ_β and μ_β are the fluid density and dynamic viscosity, while V_β is the volume occupied by the β-phase (see Fig. 1). Here and along the document, the * exponent denotes dimensional variables. For readability purpose, the notations of the differential operators, volumes and areas, and characteristic lengths are kept without exponents weather they are dimensional or dimensionless.

To proceed to up-scaling by volume averaging, the general methodology [58] is to construct an averaging volume $\mathcal{V}$ of characteristic length r_0 that verifies the length-scales separation $l_\beta \ll r_0 \ll L$ where l_β and L are the characteristics lengths of the pores and the macroscopic domain respectively (see Fig. 1). The superficial and intrinsic averages on the averaging volume $\mathcal{V}$ are defined respectively as

$$\langle \psi_\beta \rangle = \frac{1}{\mathcal{V}} \int_{V_\beta} \psi_\beta dV_\beta \quad \text{and} \quad \langle \psi_\beta \rangle^\beta = \frac{1}{V_\beta} \int_{V_\beta} \psi_\beta dV_\beta \tag{3}$$

where ψ_β is an arbitrary variable defined in the β-phase. These two definitions are related through the volume fraction of the β-phase $\varepsilon_\beta = V_\beta/\mathcal{V}$ by $\langle \psi_\beta \rangle = \varepsilon_\beta \langle \psi_\beta \rangle^\beta$. The averages of differential operators can be expressed using the following averaging theorems [58]

$$\langle \nabla \psi_\beta \rangle = \nabla \langle \psi_\beta \rangle + \frac{1}{\mathcal{V}} \int_{A_{\beta\sigma}} \mathbf{n}_{\beta\sigma} \psi_\beta dA \tag{4a}$$

$$\langle \nabla \cdot \mathbf{a}_\beta \rangle = \nabla \cdot \langle \mathbf{a}_\beta \rangle + \frac{1}{\mathcal{V}} \int_{A_{\beta\sigma}} \mathbf{n}_{\beta\sigma} \cdot \mathbf{a}_\beta dA \tag{4b}$$

where $\mathbf{a}_\beta$ is an arbitrary tensor field of order $n \geq 1$. These expressions involve surface integrals on the fluid-solid interface $A_{\beta\sigma}$ contained in $\mathcal{V}$ and thus allow to take into account the influence pore-scale boundary conditions in the averaged pore-scale equations. Moreover the presence of the local field such as ψ_β and $\mathbf{a}_\beta$ in these integrals motivates the introduction of a decomposition of the pore-scale fields using their intrinsic average and a corresponding spatial deviation [21]

$$\psi_\beta = \langle \psi_\beta \rangle^\beta + \tilde{\psi}_\beta \tag{5}$$

Making use of these definitions and following the volume averaging method [57, 58, 60, 61], one can upscale the local flow description Eqs. (2) to obtain the non-closed macroscopic transport equations

$$\nabla \cdot \langle \mathbf{v}_\beta^* \rangle^\beta = 0 \tag{6a}$$

$$\rho_\beta \langle \mathbf{v}_\beta^* \rangle^\beta \cdot \nabla \langle \mathbf{v}_\beta^* \rangle^\beta + \rho_\beta \nabla \cdot \langle \tilde{\mathbf{v}}_\beta^* \tilde{\mathbf{v}}_\beta^* \rangle^\beta = - \nabla \langle p_\beta^* \rangle^\beta + \mu_\beta \nabla^2 \langle \mathbf{v}_\beta^* \rangle^\beta + \frac{1}{V_\beta} \int_{A_{\beta\sigma}} \mathbf{n}_{\beta\sigma} \cdot \left(-\mathbf{I} \tilde{p}_\beta^* + \mu_\beta \nabla \tilde{\mathbf{v}}_\beta^* \right) dA \tag{6b}$$

The validity of the above equations relies on the assumption of homogeneous porous medium and of the scale separation ($l_\beta \ll r_0 \ll L$) [1]. Equation (6b) is not closed since the local deviations of the pressure and velocity still appear in the inertial term and in the area integral that represents the friction forces exerted by the solid phase σ on the fluid β.

In order to obtain a closed form of the averaged equations, one can write a boundary-value problem verified by the spatial deviations $\tilde{\mathbf{v}}_\beta^*$ and $\tilde{p}_\beta^*$ by subtracting the averaged problem (6) to the pore-scale equations (2), and expand the local fields using the decomposition in spatial deviations Eq. (5) [21]. After some simplifications based on the above length-scale constraints, one obtains the local deviation problem [9, 24, 56, 57]

$$\nabla \cdot \tilde{\mathbf{v}}_\beta^* = 0 \quad \text{in} \quad V_\beta \tag{7a}$$

$$\rho_\beta \mathbf{v}_\beta^* \cdot \nabla \tilde{\mathbf{v}}_\beta^* = -\nabla \tilde{p}_\beta^* + \mu_\beta \nabla^2 \tilde{\mathbf{v}}_\beta^* - \frac{1}{V_\beta} \int_{A_{\beta\sigma}} \mathbf{n}_{\beta\sigma} \cdot \left(-\mathbf{I}\tilde{p}_\beta^* + \mu_\beta \nabla \tilde{\mathbf{v}}_\beta^*\right) dA \quad \text{in} \quad V_\beta \tag{7b}$$

$$\tilde{\mathbf{v}}_\beta^* = -\langle \mathbf{v}_\beta^* \rangle^\beta \quad \text{on} \quad A_{\beta\sigma} \tag{7c}$$

$$\tilde{\mathbf{v}}_\beta^*(\mathbf{r} + \mathbf{l_i}) = \tilde{\mathbf{v}}_\beta^*(\mathbf{r}) \quad ; \quad \tilde{p}_\beta^*(\mathbf{r} + \mathbf{l_i}) = \tilde{p}_\beta^*(\mathbf{r}) \quad ; \quad i = 1, 2, 3 \tag{7d}$$

$$\langle \tilde{\mathbf{v}}_\beta^* \rangle^\beta = 0 \quad ; \quad \langle \tilde{p}_\beta^* \rangle^\beta = 0 \tag{7e}$$

where $\mathbf{l_i}$ are the periodic vector in the $\mathbf{e_i}$ direction of the periodic unit cell. Here the deviations are supposed to satisfy periodic boundary conditions. Note that this does not suppose that the porous medium is periodic, only that the local problem is solved on a representative unit cell that satisfies the length scale constraints [20, 41, 42, 58].

Since the deviation problem is defined within the averaging volume V_β, it is convenient to express the system in terms of the pore Reynolds number

$$Re_p = \frac{\rho_\beta v_{ref} \ell}{\mu_\beta} \tag{8}$$

where v_{ref} is a reference velocity constant over V_β, and ℓ is a characteristic length of the pore scale. In accordance, the dimensionless local variables and their deviations are defined as

$$\mathbf{v}_\beta = \frac{\mathbf{v}_\beta^*}{v_{ref}} \quad ; \quad p_\beta = \frac{p_\beta^* \ell}{\mu_\beta v_{ref}} \quad ; \quad \tilde{\mathbf{v}}_\beta = \frac{\tilde{\mathbf{v}}_\beta^*}{v_{ref}} \quad ; \quad \tilde{p}_\beta = \frac{\tilde{p}_\beta^* \ell}{\mu_\beta v_{ref}} \tag{9}$$

In the rest of the document, all lengths are normalized with respect to the arbitrary pore-scale length ℓ except stated otherwise. Therefore the dimensionless deviation problem takes the form

$$\nabla \cdot \tilde{\mathbf{v}}_\beta = 0 \quad \text{in} \quad V_\beta \tag{10a}$$

$$Re_p \mathbf{v}_\beta \cdot \nabla \tilde{\mathbf{v}}_\beta = -\nabla \tilde{p}_\beta + \nabla^2 \tilde{\mathbf{v}}_\beta - \frac{1}{V_\beta} \int_{A_{\beta\sigma}} \mathbf{n}_{\beta\sigma} \cdot \left(-\mathbf{I}\tilde{p}_\beta + \nabla \tilde{\mathbf{v}}_\beta\right) dA \quad \text{in} \quad V_\beta \tag{10b}$$

$$\tilde{\mathbf{v}}_\beta = -\langle \mathbf{v}_\beta \rangle^\beta \quad \text{on} \quad A_{\beta\sigma} \tag{10c}$$

[1] In fact, the scale separation should be written $l_\beta \ll r_0 \ll (L_v, L_{v2}, L_{p1})$ where L_v, L_{v2} and L_{p1} are characteristic length-scales of variation of the fields $\langle \mathbf{v}_\beta \rangle^\beta$, $\nabla\nabla\langle \mathbf{v}_\beta \rangle^\beta$ and $\nabla \langle p_\beta \rangle^\beta$ respectively. Because these length-scales are of the same order of magnitude as the characteristic length of the macroscopic domain L, assuming the separation of length-scales $l_\beta \ll r_0 \ll L$ is usually equivalent to those constraints.

$$\tilde{\mathbf{v}}_\beta(\mathbf{r}+\mathbf{l_i}) = \tilde{\mathbf{v}}_\beta(\mathbf{r}) \quad ; \quad \tilde{p}_\beta(\mathbf{r}+\mathbf{l_i}) = \tilde{p}_\beta(\mathbf{r}) \quad ; \quad i = 1,2,3 \tag{10d}$$

$$\langle \tilde{\mathbf{v}}_\beta \rangle^\beta = 0 \quad ; \quad \langle \tilde{p}_\beta \rangle^\beta = 0 \tag{10e}$$

Due to the inertial effects introduced by the term on the left hand side of Eq. (10b), the system is non-linear and non-intrinsic in the sense that it still depends on the value of the flow field. Two approaches are proposed in the next section to deal with this difficulty.

3 Determination of the Forchheimer tensor

In this section, two approaches are proposed to account for the non-linearity in the deviation problem (10) and to determine the Forchheimer tensor. First a general approach based on [24] relying on the preliminary computation of a local problem for each Reynolds and macroscopic flow orientation is detailed. Then a methodology is proposed to linearize the closure problem, eliminating the need for preliminary local computations. Finally, the value of the Forchheimer tensor computed with the two methods are compared to determine the domain of validity of the linearized approach.

3.1 The general non-linear closure problem

By analogy with the up-scaling procedure of Stokes flow where the deviation problem is linear, only the macroscopic source term in Eq. (10c) is considered to map the deviations of the velocity and pressure $\tilde{\mathbf{v}}_\beta$ and $\tilde{p}_\beta$ as [56]

$$\tilde{\mathbf{v}}_\beta = \mathbf{D} \cdot \langle \mathbf{v}_\beta \rangle^\beta \tag{11a}$$

$$\tilde{p}_\beta = \mathbf{d} \cdot \langle \mathbf{v}_\beta \rangle^\beta \tag{11b}$$

where $\mathbf{D}$ and $\mathbf{d}$ are dimensionless closure variables. Implicitly, Eqs. (11) assumes that the convective velocity is known in the inertial term of Eq. (10b). Although this might seem like a strong simplification of the non-linear closure problem, this practical approximation is widely made in the literature [1, 3, 9, 24, 36, 40, 47, 51, 52, 56, 59], resulting in good predictions of macroscopic models against DNS [10, 30, 47, 48, 50, 59] and consistent with experiments [18].

Introducing Eqs. (11) into Eqs. (6), the closed macroscopic equations describing inertial flow in a porous medium is obtained [24, 40, 56]

$$\nabla \cdot \langle \mathbf{v}^*_\beta \rangle^\beta = 0 \tag{12a}$$

$$\rho_\beta \langle \mathbf{v}^*_\beta \rangle^\beta \cdot \nabla \langle \mathbf{v}^*_\beta \rangle^\beta = -\nabla \langle p^*_\beta \rangle^\beta + \mu_\beta \nabla^2 \langle \mathbf{v}^*_\beta \rangle^\beta - \mu_\beta \mathbf{H}^{*-1}_\beta \cdot \langle \mathbf{v}^*_\beta \rangle \tag{12b}$$

The global permeability tensor $\mathbf{H}^*_\beta = \mathbf{H}_\beta \ell^2$ appears as an effective property. It is defined in its dimensionless form as

$$\varepsilon_\beta \mathbf{H}^{-1}_\beta = -\frac{1}{V_\beta} \int_{A_{\beta\sigma}} \mathbf{n}_{\beta\sigma} \cdot (-\mathbf{Id} + \nabla \mathbf{D}) \, dA \tag{13}$$

and can be related to the Forchheimer tensor $\mathbf{F}^*_\beta = \mathbf{F}_\beta$ and the intrinsic permeability tensor $\mathbf{K}^*_\beta = \mathbf{K}_\beta \ell^2$ through $\mathbf{H}^{-1}_\beta = \mathbf{K}^{-1}_\beta \cdot (\mathbf{I} + \mathbf{F}_\beta)$. Note that when the viscous diffusion term is neglected in Eq. (12b), the well known Darcy-Forchheimer equation (1) is recovered.

Introducing the closure variable Eqs. (11) into the deviation problem (10), the closure problem is obtained [56]

$$\nabla \cdot \mathbf{D} = 0 \quad \text{in} \quad V_\beta \tag{14a}$$

$$Re_p \mathbf{v}_\beta \cdot \nabla \mathbf{D} = -\nabla \mathbf{d} + \nabla^2 \mathbf{D} - \frac{1}{V_\beta} \int_{A_{\beta\sigma}} \mathbf{n}_{\beta\sigma} \cdot (-\mathbf{I}\mathbf{d} + \nabla \mathbf{D})\, dA \quad \text{in} \quad V_\beta \tag{14b}$$

$$\mathbf{D} = -\mathbf{I} \quad \text{on} \quad A_{\beta\sigma} \tag{14c}$$

$$\mathbf{D}(\mathbf{r} + \mathbf{l_i}) = \mathbf{D}(\mathbf{r}) \quad ; \quad \mathbf{d}(\mathbf{r} + \mathbf{l_i}) = \mathbf{d}(\mathbf{r}) \quad ; \quad i = 1, 2, 3 \tag{14d}$$

$$\langle \mathbf{D} \rangle^\beta = 0 \quad ; \quad \langle \mathbf{d} \rangle^\beta = 0 \tag{14e}$$

This boundary-value problem is integro-differential. To facilitate its numerical resolution, it is convenient to introduce the following change of variables

$$\mathbf{D}' = \varepsilon_\beta^{-1} (\mathbf{D} + \mathbf{I}) \cdot \mathbf{H}_\beta \quad ; \quad \mathbf{d}' = \varepsilon_\beta^{-1} \mathbf{d} \cdot \mathbf{H}_\beta \tag{15}$$

to obtain a more practical form of the closure problem

$$\nabla \cdot \mathbf{D}' = 0 \quad \text{in} \quad V_\beta \tag{16a}$$

$$Re_p \mathbf{v}_\beta \cdot \nabla \mathbf{D}' = -\nabla \mathbf{d}' + \nabla^2 \mathbf{D}' + \mathbf{I} \quad \text{in} \quad V_\beta \tag{16b}$$

$$\mathbf{D}' = \mathbf{0} \quad \text{on} \quad A_{\beta\sigma} \tag{16c}$$

$$\mathbf{D}'(\mathbf{r} + \mathbf{l_i}) = \mathbf{D}'(\mathbf{r}) \quad ; \quad \mathbf{d}'(\mathbf{r} + \mathbf{l_i}) = \mathbf{d}'(\mathbf{r}) \quad ; \quad i = 1, 2, 3 \tag{16d}$$

$$\langle \mathbf{D}' \rangle^\beta = \varepsilon_\beta^{-1} \mathbf{H}_\beta \quad ; \quad \langle \mathbf{d}' \rangle^\beta = 0 \tag{16e}$$

The closure problem (16) is non-linear and still depend on the local dimensionless velocity $\mathbf{v}_\beta$. Lasseux et *al.* [24] proposed to deal with this non-linearity by introducing the decomposition $p_\beta = \langle p_\beta \rangle^\beta + \tilde{p}_\beta$ in the local problem (2), and consider the solution of the system in a representative periodic unit cell

$$\nabla \cdot \mathbf{v}_\beta = 0 \quad \text{in} \quad V_\beta \tag{17a}$$

$$Re_p \mathbf{v}_\beta \cdot \nabla \mathbf{v}_\beta = -\nabla \tilde{p}_\beta + \nabla^2 \mathbf{v}_\beta - \nabla \langle p_\beta \rangle^\beta \quad \text{in} \quad V_\beta \tag{17b}$$

$$\mathbf{v}_\beta = 0 \quad \text{on} \quad A_{\beta\sigma} \tag{17c}$$

$$\mathbf{v}_\beta(\mathbf{r} + \mathbf{l_i}) = \mathbf{v}_\beta(\mathbf{r}) \quad ; \quad \tilde{p}_\beta(\mathbf{r} + \mathbf{l_i}) = \tilde{p}_\beta(\mathbf{r}) \quad ; \quad i = 1, 2, 3 \tag{17d}$$

$$\langle \tilde{p}_\beta \rangle^\beta = 0 \tag{17e}$$

Decomposing once more the macroscopic pressure gradient $\nabla \langle p_\beta \rangle^\beta = |\nabla \langle p_\beta \rangle^\beta| \mathbf{e}_{\nabla p}$, it is clear that this form of the local problem is dependent on three dimensionless parameters: the magnitude $|\nabla \langle p_\beta \rangle^\beta|$ and the orientation $\mathbf{e}_{\nabla p}$ of the macroscopic pressure gradient, as well as the pore Reynolds number $Re_p = \rho_\beta v_{ref} \ell / \mu_\beta$. To reduce this dependency to two parameters, the reference velocity appearing in the pore Reynolds number and the dimensionless variables is taken so that $|\nabla \langle p_\beta \rangle^\beta| = 1$, that is to say $v_{ref} = |\nabla \langle p_\beta^* \rangle^\beta| \ell^2 / \mu_\beta$ and so $Re_p = \rho_\beta |\nabla \langle p_\beta^* \rangle^\beta| \ell^3 / \mu_\beta^2$. It follows that Eq. (17b) simplifies to

$$Re_p \mathbf{v}_\beta \cdot \nabla \mathbf{v}_\beta = -\nabla \tilde{p}_\beta + \nabla^2 \mathbf{v}_\beta - \mathbf{e}_{\nabla p} \quad \text{in} \quad V_\beta \tag{18}$$

where the only source terms left are the pore Reynolds number and the flow orientation.

Knowing $\mathbf{v}_\beta$ from the solution of Eqs. (17) with (18) on a representative elementary volume, one can solve the closure problem (16b) and obtain the global permeability tensor. Note that the dimensionless local velocity field $\mathbf{v}_\beta$ depends on both the orientation of the macroscopic pressure gradient $\mathbf{e}_{\nabla p}$ appearing as a source term, and in Re_p linked to the flow intensity. Therefore the global permeability tensor also depends on these macroscopic dimensionless quantities $\mathbf{H}_\beta\left(Re_p, \mathbf{e}_{\nabla p}\right)$. The procedure to solve the general non-linear closure problem will be detailed in Section 3.3.

3.2 The linearized closure problem

In order to deal with the non-linear inertial term in the closure problem and avoid having to solve an associated local problem as presented above, an alternative approach leading to a linearized closure problem is proposed using regular perturbation theory [7, 31, 39].

Let us consider the dimensionless deviation problem (10). In the case where $Re_p = 0$, the lower limit of a purely viscous Stokes flow is recovered. This suggests to linearize the deviation problem around that special case which is already linear and self-consistent. Using regular perturbation theory, any field ψ_β in the deviation equations can be expanded as a power series around Re_p

$$\psi_\beta = \sum_{k=0}^{+\infty} \psi_{\beta k} Re_p^k \tag{19}$$

Using decomposition (19) for the spatial deviations $\tilde{\mathbf{v}}_\beta$ and $\tilde{p}_\beta$ and the local velocity $\mathbf{v}_\beta$, it is possible to convert the non-linear deviation problem (10) into countable series of linearized deviation problems for each order of the Reynolds number Re_p. The details of this linearization procedure are given in Appendix A up to order 2, although the methodology can be applied to any higher order. The main results are summarized here.

The decompositions of the velocity and deviations are introduced in the deviation problem (10), and the terms in the different orders of Reynolds number are gathered. Starting at order 0, the terms in Re_p^0 form a system of equations identical to the one obtained for a purely viscous Stokes flow. The deviations at order 0 can then be decomposed in closure variables $(\mathbf{B}, \mathbf{b})$ that are solution of the same closure system as the one for a Stokes flow. This allows to compute the intrinsic permeability tensor $\mathbf{K}_\beta$. Then at order 1, collecting the terms in Re_p^1 leads to a deviation problem which structure is similar to an inertial flow, but where the non-linear term only involves terms at order 0. Therefore it can be expressed in terms of the closure variables at order 0 and be treated as a source term. One can then decompose the deviations at order 1 in terms of new closure variables $(\mathcal{C}, \mathbf{C})$ that are the solution of a closure problem at order 1 (Eqs. (A.9)). A new effective tensor $\mathcal{H}_\beta$ can be identified as a correction of the permeability tensor at order 1. The same procedure is carried at order 2, where the non-linear term only depends on variables at lower orders and therefore can be treated as a source term. It is shown that the closure variables at order 2, defined as $(\mathscr{E}, \mathcal{E})$, are solution of a closure problem (Eqs. (A.20)), where a new effective tensor $\mathscr{J}_\beta$ correcting the permeability at order 2 is identified.

Introducing the definition of the closure variables at different orders in the power series decomposition of the velocity and pressure deviations (Eq. (19)), they can be written as expansions of the macroscopic source terms

$$\tilde{\mathbf{v}}_\beta = \mathbf{B} \cdot \langle \mathbf{v}_\beta \rangle^\beta + \mathcal{C} : Re_p \langle \mathbf{v}_\beta \rangle^\beta \langle \mathbf{v}_\beta \rangle^\beta + \mathscr{E} \vdots Re_p^2 \langle \mathbf{v}_\beta \rangle^\beta \langle \mathbf{v}_\beta \rangle^\beta \langle \mathbf{v}_\beta \rangle^\beta + ... \tag{20}$$

$$\tilde{p}_\beta = \mathbf{b} \cdot \langle \mathbf{v}_\beta \rangle^\beta + \mathbf{C} : Re_p \langle \mathbf{v}_\beta \rangle^\beta \langle \mathbf{v}_\beta \rangle^\beta + \mathcal{E} \vdots Re_p^2 \langle \mathbf{v}_\beta \rangle^\beta \langle \mathbf{v}_\beta \rangle^\beta \langle \mathbf{v}_\beta \rangle^\beta + ... \tag{21}$$

Inserting these decompositions in the non-closed macroscopic equation (6b), and identifying the corrective effective tensors at each order, the linearized form of the global permeability tensor up to second order can be written as

$$\mathbf{H}_\beta^{-1} = \mathbf{K}_\beta^{-1} \cdot \left(\mathbf{I} + Re_p \mathcal{H}_\beta \cdot \langle \mathbf{v}_\beta \rangle^\beta + Re_p^2 \mathscr{J}_\beta : \langle \mathbf{v}_\beta \rangle^\beta \langle \mathbf{v}_\beta \rangle^\beta + ... \right). \tag{22}$$

In this expression, the Forchheimer correction tensor is directly identified as

$$\mathbf{F}_\beta = Re_p \mathcal{H}_\beta \cdot \langle \mathbf{v}_\beta \rangle^\beta + Re_p^2 \mathscr{J}_\beta : \langle \mathbf{v}_\beta \rangle^\beta \langle \mathbf{v}_\beta \rangle^\beta + ... \tag{23}$$

This procedure can easily be carried at higher orders, although each additional order requires to solve a new closure problem with each time a higher dimension closure variable. It should be emphasized that, in contrast to the general non-linear approach, each of the effective tensors appearing in the definition above are obtained from the solution of closure problems that are independent of the Reynolds number and pressure gradient orientation, and thus do not require the *a priori* solution of a local flow field velocity. Therefore at the macroscopic scale, the above expression can be directly used in the average equation to determine the velocity and pressure field.

3.3 Influence of the flow intensity and orientation on the Forchheimer tensor

3.3.1 Resolution of the closure problems

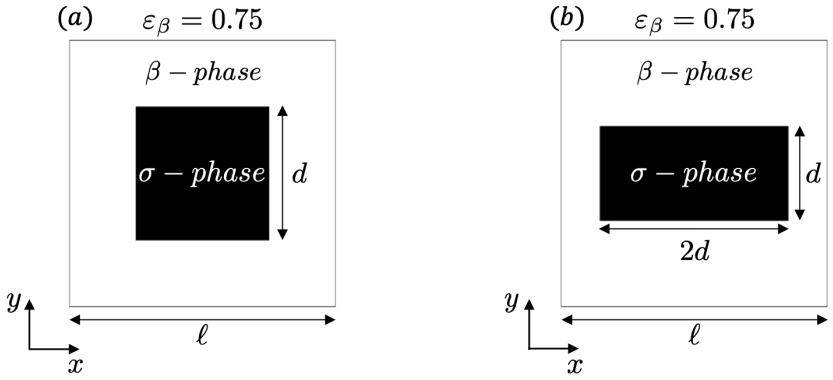

Figure 2: Example of geometries of the 2D unit cells on which the closure problems were solved (here $\varepsilon_\beta = 0.75$).

The non-linear closure problem Eqs. (16) was solved for various values of the pore Reynolds number Re_p and pressure gradient orientations $\mathbf{e}_{\nabla p}$ on the two-dimensional unit cells shown in Fig. 2. Two obstacle geometries were considered: squares and rectangles of aspect ratio 1:2. For each geometry, three volume fractions were examined ($\varepsilon_\beta = 0.25$, 0.5, and 0.75).

Concerning the linearized approach, each linearized closure problem was solved numerically in an incremental manner, starting from order 0, allowing to solve order 1, and then order 2. In this work, closure problems up to order 2 were solved in order to evaluate the global permeability

tensor from Eq. (23). Preliminary computations at orders up to 6 were performed but did not show significant improvement on the prediction of the permeability tensor within the range of validity of the linearized closure problem (data not shown).

The closure problems were solved using COMSOL Multiphysics software. The systems having the same structure as the Navier-Stokes equations, the "Laminar Flow" module was used with custom source terms added using the "Volume Force" node. For the linearized closure problem, the same mesh for the three closure problems was used in order to avoid mesh interpolations when computing the source terms.

To facilitate the comparison between the results from the two approaches, a definition of the Reynolds number based on the intrinsic permeability Re_k was used [39]

$$Re_k = \frac{\rho_\beta |\langle \mathbf{v}_\beta^* \rangle| \sqrt{k^*}}{\mu_\beta} = Re_p |\langle \mathbf{v}_\beta \rangle| \sqrt{k} \tag{24}$$

where $k = k^*/\ell^2$ is the mean of the diagonal components of the intrinsic permeability tensor $k = (K_{xx} + K_{yy})/2$, and $|\langle \mathbf{v}_\beta^* \rangle| = (\langle \mathbf{v}_\beta^* \rangle \cdot \langle \mathbf{v}_\beta^* \rangle)^{1/2} = |\langle \mathbf{v}_\beta \rangle| v_{ref}$. The flow orientation angle θ is defined such as $\mathbf{e}_{\nabla p} = \cos\theta \mathbf{e}_x + \sin\theta \mathbf{e}_y$. In all computations, dimensionless values are given with respect to the characteristic length ℓ representing the size of a unit cell (see Fig. 2).

3.3.2 Computation of the Forchheimer tensor: comparison between non-linear and linearized closure problems

The values of the xx component of the Forchheimer tensor obtained from the numerical solution of the non-linear and linearized closure problems are shown in Fig. 3 as a function of the Reynolds number and pressure gradient orientation. For Reynolds number Re_k up to about 0.1, results from the linearized closure problem are in excellent agreement with the one obtained from the non-linear problem. The component F_{xx} of the Forchheimer correction tensor shows a quadratic dependency on the Reynolds number $\mathbf{F}_\beta \sim \mathbf{A} Re_k^2$ as previously reported in the weak inertia regime [1, 24]. Notably, the linearized Forchheimer tensor (Eq. (23)) allows to express the proportionality tensor as $\mathbf{A} = \varepsilon_\beta^{-2} k^{-1} \mathscr{J}_\beta : \mathbf{e}_v \mathbf{e}_v$ where $\mathbf{e}_v = \langle \mathbf{v}_\beta \rangle^\beta / |\langle \mathbf{v}_\beta \rangle^\beta|$ is the unit vector giving the direction of the averaged velocity on the studied unit cell. This expression assumes that $\mathcal{H}_\beta$ the linearized correction tensor at order 1 is negligible, which is the case for symmetric and periodic unit cells [7, 31, 39] and is numerically verified here.

For Reynolds number between 0.1 and 1, the system enters a stronger inertia regime, and the Forcheimer tensor transitions to a linear function of the Reynolds number. Results from the linearized closure problem truncated at order 2 start to deviate from the general non-linear case in a manner that depend on the porosity and flow orientation [39]. Including higher orders for the linearization only improves marginally the range of validity compared to the non-linear closure problem (data not shown).

Fig. 3(d-f) represents the evolution of the component F_{xx} of the Forchheimer correction tensor as a function of the angle θ of the macroscopic pressure gradient for different porosities and fixed Reynolds number Re_k. The agreement between the linearized and non-linear closure problem solutions are confirmed for all flow orientations in the weak inertial regime. With increasing pore Reynolds number above 0.1 and for large porosities, discrepancies between the two approaches are observed.

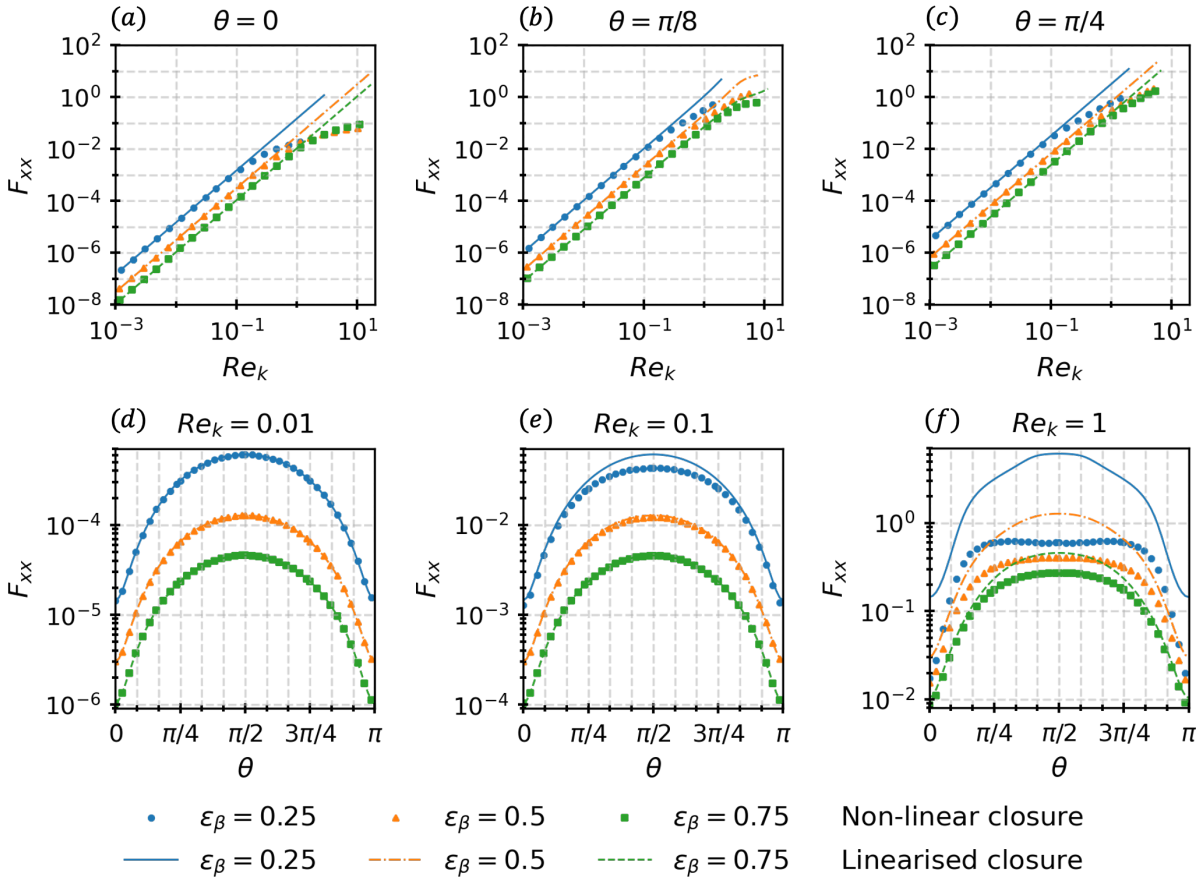

Figure 3: Comparison between non-linear and linearized component F_{xx} of the Forchheimer correction tensor for a square solid as a function of the pore Reynolds number (a-c), and as a function of the pressure gradient angle (d-f).

For completeness, the closure problems were solved on lower symmetry unit cell, namely rectangular obstacles with aspect ratio 1:2. The xx component of the Forchheimer tensor F_{xx} are shown in 4 for three different porosities as a function of the pore Reynolds number Re_k and flow orientation θ. Similarly to the square unit cell, the linearized closure problem approach shows a good agreement with the non-linear closure problem in the weak inertia regime up to $Re_k \sim 0.3$, but fails to capture the linear dependency on the Reynolds number in the strong inertia regime.

Interestingly, for low porosities ε_β, the Forchheimer correction shows a sharp maximum at pressure gradient angle θ equal to $\pi/2$. This behavior can be explained in the limit where the side of the rectangular obstacles reach the vertical boundaries of the unit cell, effectively producing a series of impermeable channels.

A comparison of the computational cost of solving the non-linear versus linear closure problems is presented in Appendix B. Briefly, the computational time required to solve the linear closure problem at order 2 is about nine time larger than for the non-linear problem. However, a single run of the linear problem gives values of the Forchheimer correction for all pore Reynold number Re_k

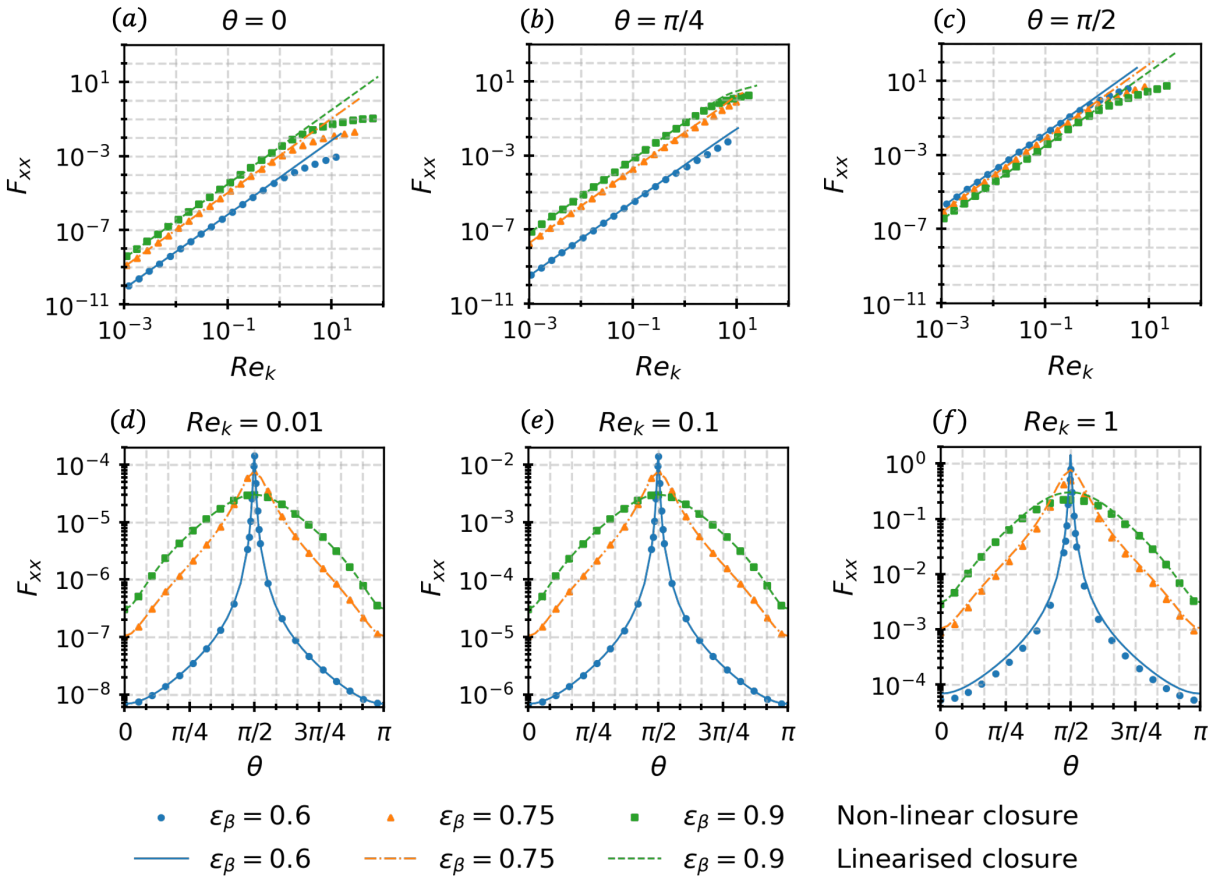

Figure 4: Comparison between non-linear and linearized component F_{xx} of the Forchheimer correction tensor for a square rectangular as a function of the pore Reynolds number (a-c), and as a function of the pressure gradient angle (d-f).

and flow orientation θ within the domain of validity. This is not the case for the non-linear problem which requires to be solved for each values of the couple (Re_k, θ). Therefore the linear closure problem is computationally advantageous when a tabulation of at least ten values of (Re_k, θ) is needed.

4 Effect of flow orientation on macroscopic inertial flow

In the previous section, the inertial correction to the permeability was computed as a function of the flow intensity and orientation. Although the linearized approach gave accurate results for a limited range in Reynolds, both approaches highlighted a non-trivial dependency of the Forchheimer tensor with the orientation of the pressure gradient. In order to explore this relationship, macroscopic simulations of the non-linear general model were performed and compared with two methods commonly used in engineering studies: direct numerical simulations (DNS) and diagonal-tensor macroscopic models.

4.1 Implementation of the macroscopic models

4.1.1 General non-linear macroscopic model

For convenience, the macroscopic transport equations (Eqs. (12a) and (12b)) are normalized with respect to a global macroscopic velocity U, representing in our case the bulk velocity imposed at the inlet of the macroscopic system. Written in their superficial form, the closed averaged equations are

$$\nabla \cdot \langle \mathbf{v}_\beta^+ \rangle = 0 \tag{25a}$$

$$\varepsilon_\beta^{-2} Re_U \langle \mathbf{v}_\beta^+ \rangle \cdot \nabla \langle \mathbf{v}_\beta^+ \rangle = -\nabla \langle p_\beta^+ \rangle^\beta + \varepsilon_\beta^{-1} \nabla^2 \langle \mathbf{v}_\beta^+ \rangle - \mathbf{H}_\beta^{-1} \cdot \langle \mathbf{v}_\beta^+ \rangle \tag{25b}$$

where the global Reynolds number is $Re_U = \rho_\beta U \ell / \mu_\beta$, $\mathbf{v}_\beta^+ = \mathbf{v}_\beta^* / U$, and $p_\beta^+ = p_\beta^* \ell / (\mu_\beta U)$. Note that because ℓ is used as the reference length scale in both the pore and global Reynolds numbers Re_p and Re_U respectively, the definition of the dimensionless effective tensor $\mathbf{H}_\beta$ remains unchanged. Additionally, it is worth noticing that the global Reynolds number Re_U reflects the effect of the macroscopic boundary conditions on the system and is constant within the whole domain, while the pore Reynolds number Re_p reflects the flow intensity and orientation at every point of the continuous macroscopic porous medium, and is therefore space dependent. This later affects the values of the effective tensor. For this reason the global permeability tensor $\mathbf{H}_\beta$ was tabulated over a range of pore Reynolds numbers and pressure gradient orientations by solving the non-linear closure problem on a two dimensional square unit cell (see Section 3.1 for details). The macroscopic transport equations (Eqs. (25)) with a space-dependent permeability tensor were then solved numerically on the macroscopic domain.

As shown in Fig. 5, three macroscopic geometries were considered: a two-dimensional straight pipe, an elbow and a diverging pipe of 1:3 expansion ratio, all partially filled with a porous medium of constant porosity $\varepsilon_{\beta 0} = 0.75$ constituted of an array of squares. A symmetry boundary condition is imposed at the top wall of the straight and diverging pipes, so that the total height of the channel in both geometries is 20ℓ at the inlet. The system is constituted of fluid domains at the inlet and outlet, and a porous domain in the center of the pipes. A fully developed parabolic flow is imposed at the entrance, while a zero pressure is imposed at the outlet, and a no-slip boundary condition is imposed at the pipe walls

$$\langle \mathbf{v}_\beta^+ \rangle = \frac{3}{2} \left(\frac{2y}{h} - \frac{y^2}{h^2} \right) \mathbf{e}_x \quad \text{at inlet} \tag{26a}$$

$$\langle p_\beta^+ \rangle^\beta = 0 \quad \text{at outlet} \tag{26b}$$

$$\langle \mathbf{v}_\beta^+ \rangle = 0 \quad \text{at pipe walls} \tag{26c}$$

with $h = 10$ the half height of the channel (see Fig. 5). As a reminder, all lengths are normalized with the pore length scale ℓ representing the size of a unit cell (see Fig. 2). Note that since the inlet and outlet are fully fluid domains, the averages are equivalent to the point fluid velocity and pressures.

In order to avoid to deal with boundary conditions at the fluid-porous interfaces, a one-domain modeling approach is adopted [10, 13, 22]. The principle is based on the observation that in the limit where the porosity tends to 1 ($\varepsilon_\beta \to 1$), the inverse of the permeability tensor tends to 0

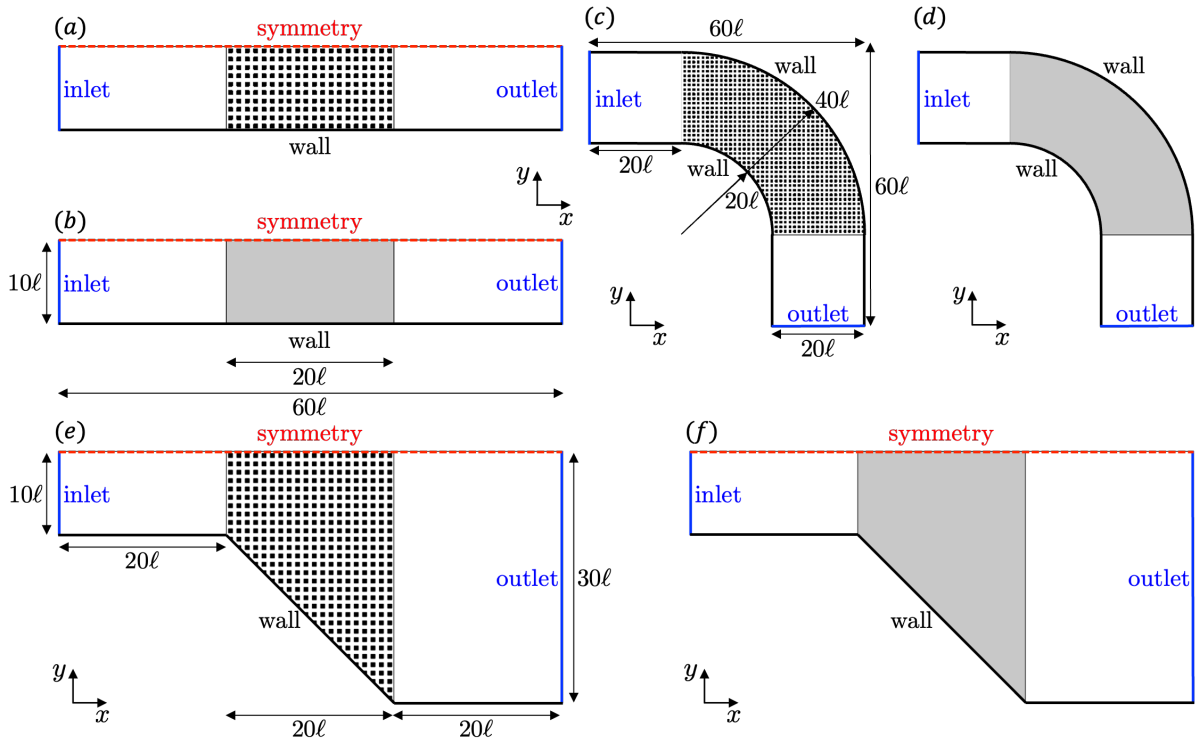

Figure 5: Geometries used for the macroscopic simulations. (a) Two-dimensional pipe partially filled with resolved square obstacles used for DNS. (b) Two-dimensional pipe partially filled with an effective continuous porous region. (c) Two-dimensional elbow partially filled with resolved square obstacles used for DNS. (d) Two-dimensional elbow partially filled with an effective continuous porous region. (e) Two-dimensional diverging pipe with expansion ratio 1:3 partially filled with resolved square obstacles used for DNS. (f) Two-dimensional diverging pipe with expansion ratio 1:3 partially filled with an effective continuous porous region.

($\mathbf{H}_\beta^{-1} \to 0$), so that the macroscopic equations (12a) and (12b) tend to the incompressible Navier-Stokes equations. Therefore they can be solved on the entire domain, provided that the porosity depends on space such as $\varepsilon_\beta(\mathbf{x}) = 1$ in the fluid region, and $\varepsilon_\beta(\mathbf{x}) = \varepsilon_{\beta 0} = 0.75$ in the porous region. To facilitate the transition from the fluid to porous regions, a smooth function of the porosity was built based on resolved fluid porous-interfaces used for direct numerical simulations (DNS) (see Fig. 5). Briefly, the space dependent porosity was defined as the cellular average of the β-phase indicator function [30, 41, 42] leading to a smooth transition of the porosity with a linear slope. Finally, to ease the evaluation of the effective permeability tensor at the fluid-porous interfacial region without having to compute it for the whole range of porosity, its values in the transition

regions was assumed to follow

$$\mathbf{H}_{\beta}^{-1}\left(\mathbf{x}\right) = \gamma_{tr}\left(\mathbf{x}\right)\mathbf{H}_{\beta}^{-1}\left(Re_p, \theta\right) \tag{27}$$

where the region-indicator function was defined as $\gamma_{tr}(\mathbf{x}) = \left[1 - \varepsilon_{\beta}(\mathbf{x})\right] / \left[1 - \varepsilon_{\beta 0}\right]$. Note that this approach can be applied only to the fluid-porous interface, but not to the solid-porous interface. To avoid singular values at the solid-porous interface, values of the region-indicator functions were computed in the bulk of the pipes/elbow and were then extrapolated using constant extrapolation through the cross-section.

4.1.2 Direct numerical simulations and diagonal tensor model

For validation, results from the general non-linear model were compared against two common approaches to model inertial flows in porous media: direct numerical simulations (DNS), and macroscopic momentum transport models with a diagonal global permeability tensor.

Direct numerical simulations (DNS) As a reference case against which to validate the results from the macroscopic models, DNS were performed. In this case, the geometric details of the porous medium are resolved (see Fig. 5a & c), and the incompressible Navier-Stokes equation are solved in the whole fluid domain including in the pore space. The same boundary conditions Eqs. (26) were applied at the inlet, outlet, and pipe walls with the averages equal to the point velocities and pressures. Additionally, a no-slip boundary condition was set at the fluid-solid interface between the fluid and the square obstacles constituting the porous medium. In order to facilitate comparisons with the homogenized macroscopic models, the velocity and pressure fields were averaged using the cellular average [16, 41–45].

Diagonal tensor model simulations As a complementary comparison, the non-linear general model was compared to a commonly used macroscopic version where the global permeability tensor is diagonal and independent of the macroscopic flow orientation [11, 37]. Such model is routinely used in state of the art CFD softwares, where instead of solving a closure problem to determine the components of the permeability tensor, an incompressible flow at a given Reynolds number is solved on a representative volume, and the diagonal components of the permeability tensor are obtained by relating the mass flow rate to the pressure drop through a simplified Darcy-Forchheimer law $\langle \mathbf{v}_{\beta}^{+} \rangle = -\mathbf{H}_{\beta}(Re_p) \cdot \nabla \langle p_{\beta}^{+} \rangle^{\beta}$.

4.1.3 Numerical implementation

All models were solved numerically using the finite element commercial software COMSOL Multiphysics 6.1 with the "Laminar Flow" module. The additional macroscopic terms were implemented as volume forces in order to obtain their values iteratively in the domain. For the general non-linear macroscopic model, the values of the inertial permeability tensor were tabulated *a priori* using the results of the non-linear general closure problem. The tabulated values were interpolated linearly with respect to the pore Reynolds number and the angle of the superficial averaged velocity.

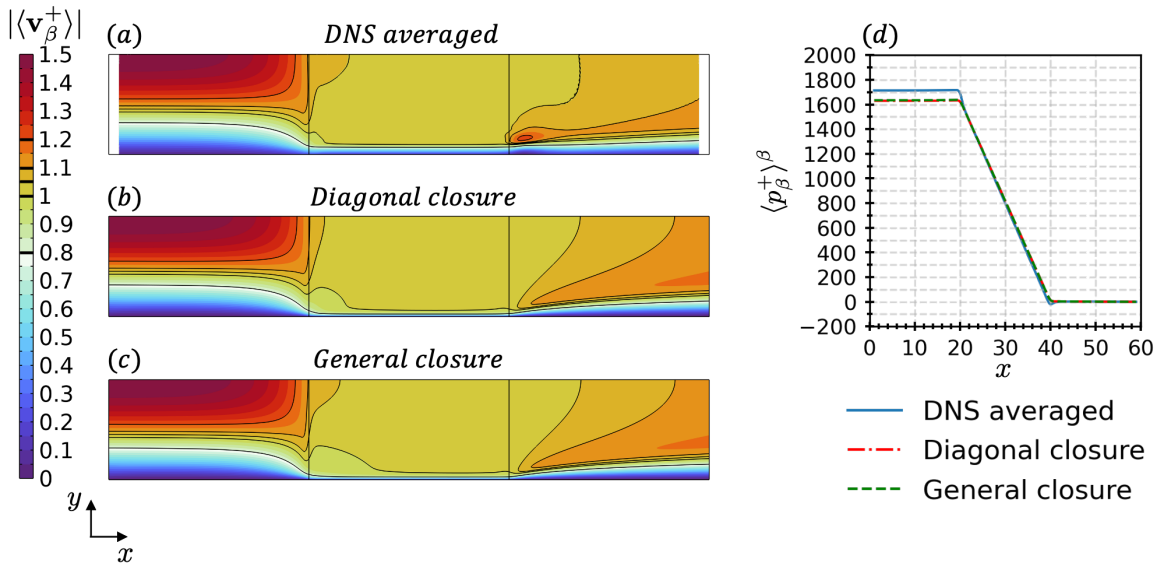

Figure 6: Comparison of macroscopic results of an inertial flow at global Reynolds number $Re_U = 30$ in a pipe partially filled with a porous medium constituted of square obstacles of porosity $\varepsilon_\beta = 0.75$. (a) Magnitude of the cellular average of the velocity field obtained from DNS. (b) Magnitude of the superficial average of the velocity field obtained from the diagonal tensor model. (c) Magnitude of the superficial average of the velocity field obtained from the general non-linear model. (d) Cross section average pressure (cellular for DNS, intrinsic for homogenized models) as a function of x.

4.2 Macroscopic simulation results

Macroscopic simulations of inertial flows in conduits filled with porous media were first performed for validation in a straight pipe filled with a porous medium. Then, to assess the influence of the extra-diagonal terms and of the macroscopic pressure gradient orientation on the global permeability tensor, an elbow filled with porous medium was considered. In all cases, values of the global Reynolds number $Re_U = \rho_\beta U \ell / \mu_\beta$ were tested for 1, 10, 30, and 50. Finally, a diverging pipe geometry was considered.

4.2.1 Inertial flow in a straight pipe partially filled with a porous medium

Fig. 6 compares the simulations results from the three models for of an inertial flow with global Reynolds number $Re_U = 30$ in a two-dimensional pipe partially filled with a porous medium. The averaged DNS simulations hold as the reference against which the homogenized models, namely the diagonal tensor model and the general non-linear model, are compared. As seen in Fig. 6, very little difference is observed between the models. All three models show a very good agreement in the inlet fluid region, validating the use of the one-domain approach to describe the fluid part. In the central porous region, the flow becomes uniform. It can be noticed that the two homogenized models slightly under-predict the thickness of the wall boundary layer at the porous-solid interface compared to DNS. Finally, in the outlet fluid region, although the homogenized models capture the overall flow behavior, they fail to predict the small recirculation zone at the corner between

Table 1: Dimensionless pressure loss between inlet and outlet of a pipe partially filled with a porous medium as a function for different values of the global Reynolds numbers for DNS and the two homogenized models.

	$\Delta\langle p_\beta^+\rangle^\beta$			Relative difference to DNS (%)	
Re_U	DNS	Diag. tensor	Gen. non-linear	Diag. tensor	Gen. non-linear
0	1618	1566	1566	3.2	3.2
1	1618	1566	1566	3.2	3.2
10	1641	1583	1583	3.5	3.5
30	1714	1630	1634	4.9	4.7
50	1771	1657	1668	6.5	5.8

the fluid-porous interface and the wall, as predicted by DNS. These limitations of the homogenized models are due to the difficulty to define a representative elementary volume that satisfies the length-scale separation close to a wall or a fluid interface. Although some jump conditions have been proposed for two-domain approaches [5,6,8,33–35], these are generally limited to non-inertial flows. More recently a methodology to account for the influence of porous media macroscopic boundaries on inertial flows was proposed [50] . Such model refinements are out of the scope of the current study.

As seen in Fig. 6d, the evolution of the cross section average of the pressure as a function of the distance from the entrance also show very similar results between the three models, although both homogenized models slightly under-predict the inlet pressure by less than 5% compared to DNS. Given that the outlet pressure is set to zero, these results point to the fact that the homogenized models underestimate the singular head losses at the fluid-porous interfaces and the distributed head-losses at the porous-wall interfaces, leading to an overall lower pressure loss between the inlet and outlet.

Simulations for various global Reynolds number up to $Re_U = 50$ were performed, giving the same qualitative behavior as for the case $Re_U = 30$ (data not shown). For completeness, the total pressure drop and their relative difference with the DNS results are summarized in Table 1. Relative differences in pressure losses of the two homogenized models compared to DNS remain lower than 7% for all the cases considered, confirming the relevance of these models. The general non-linear model and diagonal tensor models are equivalent at low global Reynolds number, with a relative difference in pressure loss compared to DNS remaining blow 3.5% for $Re_U = 10$. This relative difference in pressure loss increases with larger values of the Reynolds number, with the diagonal tensor model having larger differences than the general non-linear model. This discrepancy can be explained by the appearance of recirculation zones with increasing Reynolds numbers, leading to local streamlines having a non-zero angle with the x-axis. Although the influence of flow orientation in the unit cell is accounted for in the general non-linear model during the determination of the effective permeability tensor, this is not the case in the diagonal tensor model.

To investigate further the effect of flow orientation on inertial flow in porous media, an elbow partially filled with a porous medium is considered in the next section.

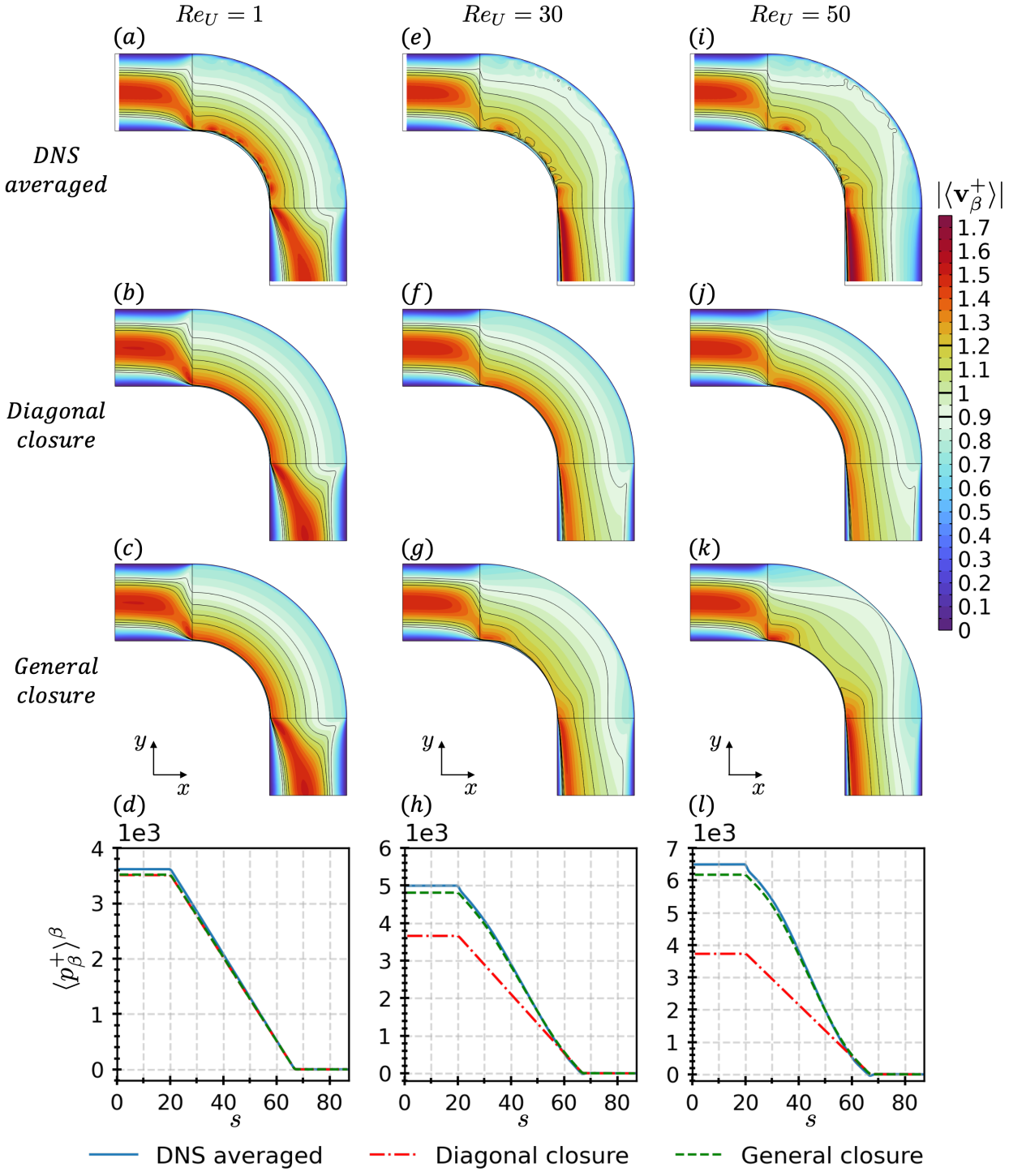

Figure 7: Comparison of macroscopic results of inertial flows in a 90° elbow partially filled with a porous medium constituted of square obstacles of porosity $\varepsilon_\beta = 0.75$. Results are shown for three global Reynolds numbers: (a, d, g, j) $Re_U = 1$, (b, e, h, k) $Re_U = 30$, (c,f, i, l) $Re_U = 50$. (a-c) Magnitude of the cellular average of the velocity field obtained from DNS. (d-f) Magnitude of the superficial average of the velocity field obtained from the diagonal tensor model. (g-i) Magnitude of the superficial average of the velocity field obtained from the general non-linear model. (j-l) Cross section average pressure (cellular for DNS, superficial for homogenized models) as a function of the arclength s.

4.2.2 Inertial flow in an elbow partially filled with a porous medium

In order to test the importance of the pressure gradient orientation on the macroscopic inertial flow in a porous medium, the three models were solved in a 90° elbow partially filled with a porous medium (see Fig. 5c & d). Importantly, the porous medium is the same as the one used in the straight pipe, namely square obstacles of porosity $\varepsilon_\beta = 0.75$ where the unit cell geometry is not rotated to follow the curvature of the domain. As a consequence, the angle between the average flow and the x-axis of the square obstacle varies from 0° at the entrance of the porous medium to $-90°$ at its exit.

Comparison between the results obtained by DNS, the diagonal-tensor macroscopic model, and the general non-linear macroscopic model are presented in Fig. 7 for global Reynolds number of $Re_U = 1$, 30, and 50. At $Re_U = 1$, the velocity profiles obtained for the macroscopic simulations are very similar to the one obtained from averaged DNS. Although averaged DNS results show some oscillations in average velocity field close to the walls due the contact of some solid obstacles with the wall, overall the three simulations predict a constant averaged velocity profile along the length of the porous region. For larger global Reynolds numbers of $Re_U = 30$ and 50, inertial effects induce variations of the average velocity profile along the length of the elbow, as shown by the averaged DNS (Fig. 7e & i). This behavior is not captured by the diagonal tensor model which predicts a constant average velocity profile in each section of the porous region (Fig. 7f & j). In contrast, the general non-linear model does reproduce well the non-uniform velocity profile predicted by DNS (Fig. 7g & k). The difference between the predictions of the two homogenized model increases with the global Reynolds number as inertial effects become more and more present. Interestingly, it is clear from the streamlines at $Re_U = 30$ and 50 that the inertial flow follows preferential paths at angles $\theta = 0$, $\pi/4$, and $\pi/2$ as shown in the DNS and general closure model. This is due to the choice of the unit cell geometry with the regular arrangement of square obstacles.

The difference of predictions between the homogenized models is even more evident from the values of the averaged intrinsic pressures. The evolution of the cross-section averaged pressure along the length of the elbow is shown in Fig. 7d, h, & l, and the values of the pressure losses and relative difference to DNS are given in Table 2. As inertial effects increase, both DNS and the general non-linear model predict a significantly larger pressure loss between the inlet and outlet (more than a 40% increase in pressure at $Re_U = 50$ compared to $Re_U = 1$), as well as a deviation from a linear pressure evolution in the porous region. In contrast, the diagonal tensor model only predicts a mild increase in pressure (about 5% at $Re_U = 50$ compared to $Re_U = 1$) and maintains a linear decrease in pressure along the elbow. Importantly, in the fully inertial regime, the general non-linear model remains within the 5% of the pressure drop predicted by DNS, while the diagonal tensor model shows differences up to 42.6% at $Re_U = 50$.

The ability of the general non-linear model to capture realistically the variation of average velocity field along the elbow is due to the dependency of the global permeability tensor on the pressure gradient orientation. Indeed, in the elbow the flow is diverted by a 90° angle while the unit cell geometry remains with the same orientation. As a consequence, the global permeability tensor displays non-negligible extra-diagonal terms and a dependency of its components to the flow orientation compared to the unit cell geometry. While these two features are accounted for in the general non-linear model, they are not captured in the diagonal tensor model which fails to account for the change of tortuosity and permeability (including inertial corrections) induced by the change

Table 2: Pressure loss between inlet and outlet of a 90° elbow partially filled with a porous medium as a function for different values of the global Reynolds numbers for DNS and the two homogenized models.

	$\Delta\langle p_\beta^+\rangle^\beta$			Relative difference to DNS (%)	
Re_U	DNS	Diag. tensor	Gen. non-linear	Diag. tensor	Gen. non-linear
0	3611	3508	3508	2.8	2.8
1	3617	3510	3519	3.0	2.7
10	3846	3550	3729	7.7	3.0
30	4995	3659	4811	26.8	3.7
50	6491	3727	6173	42.6	4.9

of flow orientation relative to the pore unit geometry.

4.2.3 Inertial flow in a diverging pipe partially filled with a porous medium

Finally, a diverging pipe filled with a porous medium is considered (see Fig. 5e-f). A Reynolds number of $Re_U = 50$ is imposed at the entrance to ensure a strong inertial but laminar flow regime. As seen in Fig. 8, the general observations on the different macroscopic models are similar to the ones from the elbow geometry: the diagonal model fails to capture the change of average velocity orientation and predicts a more uniform flow field than the one obtained with the general closure model which is much closer to DNS results. Some discrepancies between the general model and DNS remain, particularly near the pipe walls due to the macroscopic boundary layer and at the fluid/porous interfaces. Once again, the evolution of the section average pressure along the channel shows that the diagonal model largely under-predicts the head loss (19.5% difference with DNS) while the general model successfully predicts the head loss within 3.05% of the DNS values.

5 Conclusion

Incompressible inertial flows in porous media are well described by the Forchheimer equation, where inertial effects are accounted for through a corrective tensor $\mathbf{F}_\beta$ to the intrinsic permeability. Using up-scaling techniques such as the volume averaging method [24, 56], one can compute the effective tensor from the solution of a non-linear closure problem on a representative unit cell. However this closure problem requires that, for each flow orientation and for each pore Reynolds number, an associated local problem must be solved before solving the non-linear closure problem. To deal with this difficulty, in this work, a linearized approach where the resulting linear closure problems are independent of the flow orientation was proposed and assessed. Then, macroscopic simulations were carried to study the importance of the macroscopic flow orientation, highlighting the importance of extra-diagonal components in the Forchheimer correction tensor.

The non-linear closure problem obtained with the volume averaging method [24] was linearized into a series of linear problems independent of the macroscopic flow orientation. This procedure is a generalization of previous works for weakly inertial flows [7, 31, 39] leading to linear and intrinsic closure problems independent of the macroscopic flow orientation. Developments were pushed up to order 2 with respect to the pore Reynolds number, resulting in a Forchheimer correction expressed as a quadratic polynomial of Re_k. The limit of validity of this approach was assessed by comparison

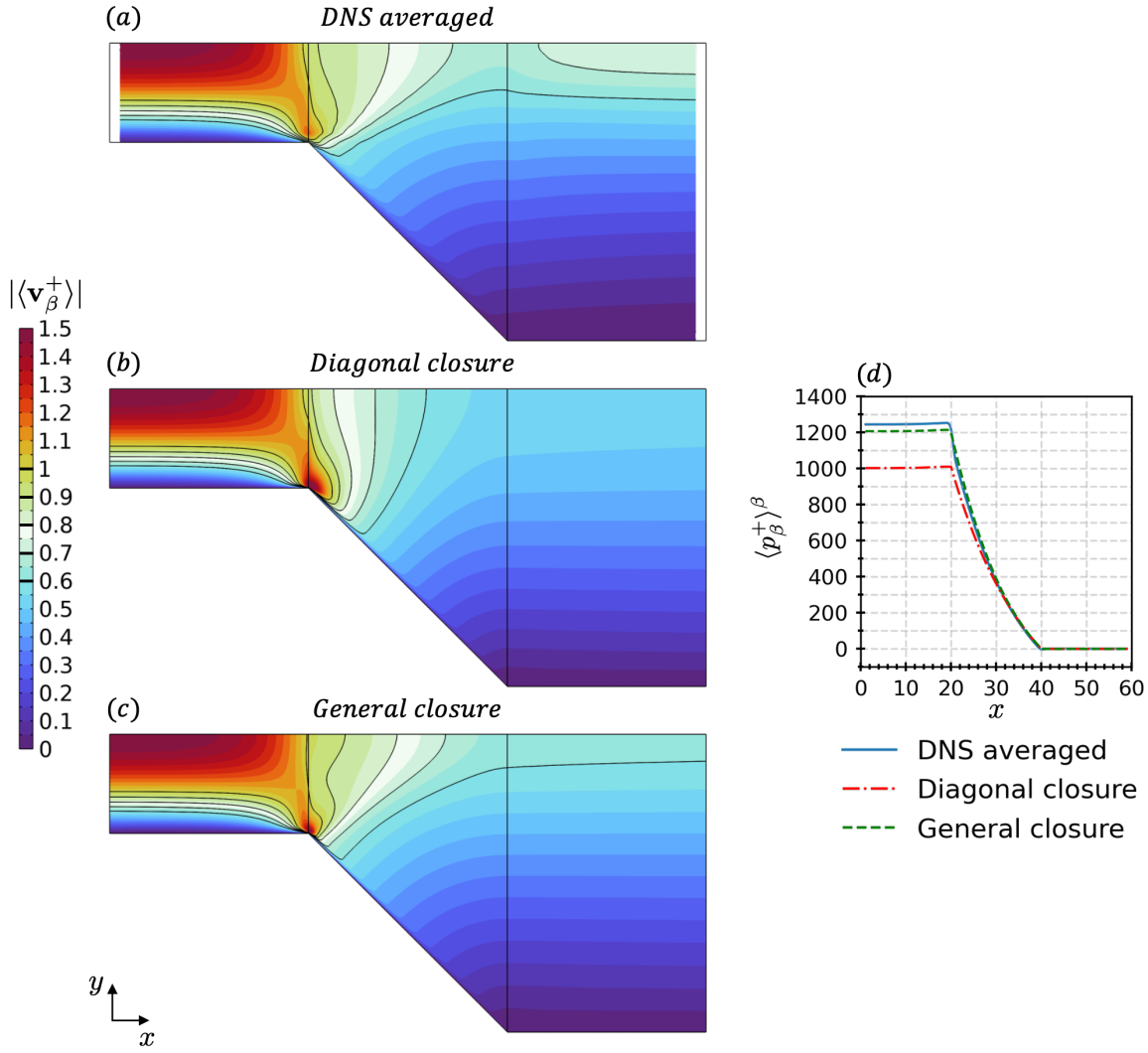

Figure 8: Comparison of macroscopic results of an inertial flow at global Reynolds number $Re_U = 50$ in a diverging pipe with expansion ratio 1:3, partially filled with a porous medium constituted of square obstacles of porosity $\varepsilon_\beta = 0.75$. (a) Magnitude of the cellular average of the velocity field obtained from DNS. (b) Magnitude of the superficial average of the velocity field obtained from the diagonal tensor model. (c) Magnitude of the superficial average of the velocity field obtained from the general non-linear model. (d) Cross section average pressure (cellular for DNS, intrinsic for homogenized models) as a function of x.

with a general non-linear closure problem. The effect of flow orientation and intensity was studied for different square and rectangle unit cell geometries, showing a good match between the linearized

and general non-linear models up to pore Reynolds number Re_k of the order one. The linearized quadratic model was able to accurately predict the weak inertia regime [2, 23, 24, 39] for different flow orientations. The generality of the presented method allows to expand to higher orders, but at the cost of increasing tensor order leading to exponential numerical difficulties.

To assess the effect of flow orientation on the extra-diagonal terms of the correction tensor, macroscopic simulations were conducted for Reynolds number up to 50 in straight and 90° elbow conduits filled with porous media. Results from the macroscopic general non-linear model were compared against a diagonal macroscopic model commonly used in engineering applications [11, 37, 53]. In the straight conduit, due to the flow orientation being constant, no significant difference were observed between diagonal and general non-linear models. However, in the case where the flow orientation varies along the elbow conduit, the diagonal model was unable to predict the non-homogeneous velocity field along the channel's length, leading to a under-prediction of the pressure loss by more than 40% at $Re_U = 50$ compared to DNS. In contrast, the general diagonal model captured well the average velocity field, and predicted a pressure loss within 5% of the values obtained by DNS. Qualitatively similar conclusions were obtained on a diverging pipe reproducing a progressive expansion flow.

All together, this work highlights the importance of macroscopic pressure orientation on the global permeability tensor in inertial flow in porous media. Further developments to improve the prediction of the macroscopic inertial flow include introducing accurate jump conditions [5, 6, 8] or profile transition at fluid-porous and solid-porous interfaces [10, 22, 33, 48–50]. Concerning the proposed linearization approach, future applications to transfers where the critical phenomenon occurs with a dimensionless number below one might be particularly relevant, such as in weakly compressible and dilatable flows.

References

[1] M. Agnaou, D. Lasseux, and A. Ahmadi. From steady to unsteady laminar flow in model porous structures: an investigation of the first Hopf bifurcation. *Computers and Fluids*, 136:67–82, June 2016. hal-01329941.

[2] M. Agnaou, D. Lasseux, and A. Ahmadi. Origin of the inertial deviation from Darcy's law: An investigation from a microscopic flow analysis on two-dimensional model structures. *Physical Review E*, 96(043105), Oct. 2017.

[3] C. Aguilar-Madera, J. Flores-Cano, V. Matías-Pérez, J. Briones-Carrillo, and F. Velasco-Tapia. Computing the permeability and Forchheimer tensor of porous rocks via closure problems and digital images. *Advances in Water Resources*, 142:103616, Aug. 2020.

[4] A. A. Alshare, T. W. Simon, and P. J. Strykowski. Simulations of flow and heat transfer in a serpentine heat exchanger having dispersed resistance with porous-continuum and continuum models. *International Journal of Heat and Mass Transfer*, 53(5):1088–1099, Feb. 2010.

[5] P. Angot, B. Goyeau, and J. A. Ochoa-Tapia. Asymptotic modeling of transport phenomena at the interface between a fluid and a porous layer: Jump conditions. *Physical Review E*, 95(6):063302, June 2017.

[6] P. Angot, B. Goyeau, and J. A. Ochoa-Tapia. A nonlinear asymptotic model for the inertial flow at a fluid-porous interface. *Advances in Water Resources*, 149:103798, Mar. 2021.

[7] M. Balhoff, A. Mikelić, and M. F. Wheeler. Polynomial Filtration Laws for Low Reynolds Number Flows Through Porous Media. *Transport in Porous Media*, 81(1):35–60, Jan. 2010.

[8] G. S. Beavers and D. D. Joseph. Boundary conditions at a naturally permeable wall. *Journal of Fluid Mechanics*, 30(1):197–207, Oct. 1967.

[9] P. Bousquet-Melou, B. Goyeau, M. Quintard, F. Fichot, and D. Gobin. Average momentum equation for interdendritic flow in a solidifying columnar mushy zone. *International Journal of Heat and Mass Transfer*, 45(17):3651–3665, Aug. 2002.

[10] C.-H. Bruneau, D. Lasseux, and F. J. Valdés-Parada. Comparison between direct numerical simulations and effective models for fluid-porous flows using penalization. *Meccanica*, 55(5):1061–1077, May 2020.

[11] G. Buckinx and M. Baelmans. Multi-scale modelling of flow in periodic solid structures through spatial averaging. *Journal of Computational Physics*, 291:34–51, June 2015.

[12] M. Chandesris, G. Serre, and P. Sagaut. A macroscopic turbulence model for flow in porous media suited for channel, pipe and rod bundle flows. *International Journal of Heat and Mass Transfer*, 49(15):2739–2750, July 2006.

[13] H. Chen and X.-P. Wang. A one-domain approach for modeling and simulation of free fluid over a porous medium. *Journal of Computational Physics*, 259:650–671, Feb. 2014.

[14] M. Cochennec, H. Davarzani, Y. Davit, S. Colombano, I. Ignatiadis, G. Masselot, and M. Quintard. Impact of gravity and inertia on stable displacements of DNAPL in highly permeable porous media. *Advances in Water Resources*, 162:104139, Apr. 2022.

[15] H. Darcy. *Les fontaines publiques de la ville de Dijon: Exposition et application des principes à suivre et des formules à employer dans les questions de distribution d'eau : Ouvrage terminé par un appendice relatif aux fournitures d'eau de plusieurs villes, au filtrage des eaux et à la fabrication des tuyaux de fonte, de plomb, de tôle et de bitume*. V. Dalmont, Paris, 1856.

[16] Y. Davit and M. Quintard. Technical Notes on Volume Averaging in Porous Media I: How to Choose a Spatial Averaging Operator for Periodic and Quasiperiodic Structures. *Transport in Porous Media*, 119(3):555–584, Sept. 2017.

[17] Y. Davit and M. Quintard. One-Phase and Two-Phase Flow in Highly Permeable Porous Media. *Heat Transfer Engineering*, 40(5-6):391–409, Apr. 2019.

[18] S. Ergun. Fluid flow through packed columns. 48(2):89.

[19] P. Forchheimer. Wasserbewegung durch Boden. *Z. Ver. Deutsch, Ing.*, 45:1782–1788, 1901.

[20] T. O. M. Forslund, I. A. S. Larsson, J. G. I. Hellström, and T. S. Lundström. The Effects of Periodicity Assumptions in Porous Media Modelling. *Transport in Porous Media*, 137(3):769–797, Apr. 2021.

[21] W. G. Gray. A derivation of the equations for multi-phase transport. *Chemical Engineering Science*, 30(2):229–233, Feb. 1975.

[22] R. Hernandez-Rodriguez, P. Angot, B. Goyeau, and J. A. Ochoa-Tapia. Momentum transport in the free fluid-porous medium transition layer: one-domain approach. *Chemical Engineering Science*, 248:117111, Feb. 2022.

[23] Z. Khalifa, L. Pocher, and N. Tilton. Regimes of flow through cylinder arrays subject to steady pressure gradients. *International Journal of Heat and Mass Transfer*, 159:120072, Oct. 2020.

[24] D. Lasseux, A. A. Abbasian Arani, and A. Ahmadi. On the stationary macroscopic inertial effects for one phase flow in ordered and disordered porous media. *Physics of Fluids*, 23(7):073103, July 2011.

[25] D. Lasseux, F. J. Valdès-Parada, and F. Bellet. Macroscopic model for unsteady flow in porous media. *Journal of Fluid Mechanics*, 862:283–311, Mar. 2019.

[26] D. Lasseux and F. J. Valdés-Parada. On the developments of Darcy's law to include inertial and slip effects. *Comptes Rendus Mécanique*, 345(9):660–669, Sept. 2017.

[27] D. Lasseux, F. J. Valdés-Parada, and A. Bottaro. Upscaled model for unsteady slip flow in porous media. *Journal of Fluid Mechanics*, 923:A37, Sept. 2021.

[28] M. Lemos. *Turbulence in Porous Media*. Elsevier, 2012.

[29] Z.-z. Li, Y.-d. Ding, Q. Liao, M. Cheng, and X. Zhu. An approach based on the porous media model for numerical simulation of 3D finned-tubes heat exchanger. *International Journal of Heat and Mass Transfer*, 173:121226, July 2021.

[30] N. Luminari, G. A. Zampogna, C. Airiau, and A. Bottaro. A penalization method to treat the interface between a free-fluid region and a fibrous porous medium. *Journal of Porous Media*, 22(9):1095–1107, 2019.

[31] C. C. Mei and J.-L. Auriault. The effect of weak inertia on flow through a porous medium. *Journal of Fluid Mechanics*, 222:647–663, Jan. 1991.

[32] D. Missirlis, S. Donnerhack, O. Seite, C. Albanakis, A. Sideridis, K. Yakinthos, and A. Goulas. Numerical development of a heat transfer and pressure drop porosity model for a heat exchanger for aero engine applications. *Applied Thermal Engineering*, 30(11):1341–1350, Aug. 2010.

[33] S. B. Naqvi and A. Bottaro. Interfacial conditions between a free-fluid region and a porous medium. *International Journal of Multiphase Flow*, 141:103585, Aug. 2021.

[34] J. Ochoa-Tapia and S. Whitaker. Momentum transfer at the boundary between a porous medium and a homogeneous fluid—II. Comparison with experiment. *International Journal of Heat and Mass Transfer*, 38(14):2647–2655, Sept. 1995.

[35] J. A. Ochoa-Tapia and S. Whitaker. Momentum transfer at the boundary between a porous medium and a homogeneous fluid—I. Theoretical development. *International Journal of Heat and Mass Transfer*, 38(14):2635–2646, Sept. 1995.

[36] S. Pasquier, M. Quintard, and Y. Davit. Modeling flow in porous media with rough surfaces: effective slip boundary conditions and application to structured packings. *Chemical Engineering Science*, vol. 165:pp. 131–146, 2017.

[37] S. V. Patankar, C. H. Liu, and E. M. Sparrow. Fully Developed Flow and Heat Transfer in Ducts Having Streamwise-Periodic Variations of Cross-Sectional Area. *Journal of Heat Transfer*, 99(2):180–186, May 1977.

[38] M. Pauthenet. *Macroscopic model and numerical simulation of elastic canopy flows.* PhD thesis, Institut National Polytechnique de Toulouse - INPT, Sept. 2018.

[39] M. Pauthenet, Y. Davit, M. Quintard, and A. Bottaro. Inertial Sensitivity of Porous Microstructures. *Transport in Porous Media*, 125, Nov. 2018.

[40] C. T. Paéz-García, F. J. Valdés-Parada, and D. Lasseux. Macroscopic momentum and mechanical energy equations for incompressible single-phase flow in porous media. *Physical Review E*, 95, Feb. 2017.

[41] M. Quintard and S. Whitaker. Transport in ordered and disordered porous media I: The cellular average and the use of weighting functions. *Transport in Porous Media*, 14(2):163–177, Feb. 1994.

[42] M. Quintard and S. Whitaker. Transport in ordered and disordered porous media II: Generalized volume averaging. *Transport in Porous Media*, 14(2):179–206, Feb. 1994.

[43] M. Quintard and S. Whitaker. Transport in ordered and disordered porous media III: Closure and comparison between theory and experiment. *Transport in Porous Media*, 15(1):31–49, Apr. 1994.

[44] M. Quintard and S. Whitaker. Transport in ordered and disordered porous media. IV: computer generated porous media for three-dimensional systems. Transp. Porous Media 15(1), 51-70. *Transport in Porous Media*, 15:51–70, Apr. 1994.

[45] M. Quintard and S. Whitaker. Transport in ordered and disordered porous media V: Geometrical results for two-dimensional systems. *Transport in Porous Media*, 15(2):183–196, May 1994.

[46] M. Schmid, G. Lawrence, M. Parlange, and M. Giometto. Volume Averaging for Urban Canopies. *Boundary-Layer Meteorology*, 173, Dec. 2019.

[47] C. Soulaine and M. Quintard. On the use of a Darcy–Forchheimer like model for a macro-scale description of turbulence in porous media and its application to structured packings. *International Journal of Heat and Mass Transfer*, 74:88–100, July 2014.

[48] F. Valdés-Parada and D. Lasseux. A novel one-domain approach for modeling flow in a fluid-porous system including inertia and slip effects. *Physics of Fluids*, 33(2):022106, Feb. 2021.

[49] F. J. Valdés-Parada, B. Goyeau, and J. A. Ochoa-Tapia. Jump momentum boundary condition at a fluid–porous dividing surface: Derivation of the closure problem. *Chemical Engineering Science*, 62(15):4025–4039, Aug. 2007.

[50] F. J. Valdés-Parada and D. Lasseux. Flow near porous media boundaries including inertia and slip: A one-domain approach. *Physics of Fluids*, 33(7):073612, July 2021.

[51] F. J. Valdés-Parada, D. Lasseux, and F. Bellet. A new formulation of the dispersion tensor in homogeneous porous media. *Advances in Water Resources*, 90:70–82, Apr. 2016.

[52] Y. Wang, A. Ahmadi, and D. Lasseux. On the Inertial Single Phase Flow in 2D Model Porous Media: Role of Microscopic Structural Disorder. *Transport in Porous Media*, 128(1):201–220, Feb. 2019.

[53] Z. Wang, H. Shang, and J. Zhang. Lattice Boltzmann simulations of heat transfer in fully developed periodic incompressible flows. *Physical Review E*, 95(6):063309, June 2017.

[54] E. G. Ward and C. Dalton. Strictly Sinusoidal Flow Around a Stationary Cylinder. *Journal of Basic Engineering*, 91(4):707–713, Dec. 1969.

[55] S. Whitaker. Flow in porous media I: A theoretical derivation of Darcy's law. *Transport in Porous Media*, 1(1):3–25, 1986.

[56] S. Whitaker. The Forchheimer equation: A theoretical development. *Transport in Porous Media*, 25:27–61, Sept. 1996.

[57] S. Whitaker. Volume averaging of transport equations. *International Series On Advances In Fluid Mechanics*, 13:1–60, 1997.

[58] S. Whitaker. *The Method of Volume Averaging*, volume 13 of *Theory and Applications of Transport in Porous Media*. Springer Netherlands, Dordrecht, 1999.

[59] B. Wood, X. He, and S. Apte. Modeling Turbulent Flows in Porous Media. *Annual Review of Fluid Mechanics*, 52, Jan. 2020.

[60] B. D. Wood. The role of scaling laws in upscaling. *Advances in Water Resources*, 32(5):723–736, May 2009.

[61] B. D. Wood and F. J. Valdés-Parada. Volume averaging: Local and nonlocal closures using a Green's function approach. *Advances in Water Resources*, 51:139–167, Jan. 2013.

Statements and declarations

The authors acknowledge support from the Association Nationale Recherche Technologie (ANRT) during the preparation of the manuscript.

All authors contributed to the study conception and design. Numerical simulations were performed by YB. The initial draft of the manuscript was written by YB, MC, and BG, and all authors commented on previous versions of the manuscript. All authors read and approved the final manuscript.

APPENDIX

A Linearization of the closure problem associated with inertial flow

Based on regular perturbation theory, any field ψ_β in the deviation problem (10) is expanded as a power series around Re_p

$$\psi_\beta = \sum_{k=0}^{+\infty} \psi_{\beta k} Re_p^k \tag{A.1}$$

This leads to a self-sufficient series of linear deviation problems for each order of the Reynolds number Re_p. Here the details of their derivation and the procedure to obtain the corresponding closure problem are detailed up to order 2, although the methodology can be easily applied to higher orders.

Order k = 0

First, the closure problem at order 0 is developed as the reference case of the linearization. This corresponds to the limit case where $Re_p = 0$

$$\nabla \cdot \tilde{\mathbf{v}}_{\beta 0} = 0 \quad \text{in} \quad V_\beta \tag{A.2a}$$

$$0 = -\nabla \tilde{p}_{\beta 0} + \nabla^2 \tilde{\mathbf{v}}_{\beta 0} - \frac{1}{V_\beta} \int_{A_{\beta\sigma}} \mathbf{n}_{\beta\sigma} \cdot \left(-\mathbf{I}\tilde{p}_{\beta 0} + \nabla \tilde{\mathbf{v}}_{\beta 0}\right) dA \quad \text{in} \quad V_\beta \tag{A.2b}$$

$$\tilde{\mathbf{v}}_{\beta 0} = -\langle \mathbf{v}_{\beta 0} \rangle^\beta \quad \text{on} \quad A_{\beta\sigma} \tag{A.2c}$$

$$\tilde{\mathbf{v}}_{\beta 0}\left(\mathbf{r} + \mathbf{l_i}\right) = \tilde{\mathbf{v}}_{\beta 0}\left(\mathbf{r}\right) \quad ; \quad \tilde{p}_{\beta 0}\left(\mathbf{r} + \mathbf{l_i}\right) = \tilde{p}_{\beta 0}\left(\mathbf{r}\right) \quad ; \quad i = 1, 2, 3 \tag{A.2d}$$

$$\langle \tilde{\mathbf{v}}_{\beta 0} \rangle^\beta = 0 \quad ; \quad \langle \tilde{p}_{\beta 0} \rangle^\beta = 0 \tag{A.2e}$$

which is exactly the spatial deviation problem for a Stokes flow at the pore-scale. Because it is linear and self-consistent, it is possible to use the superposition principle to express the spatial deviations $\tilde{\mathbf{v}}_{\beta 0}$ and $\tilde{p}_{\beta 0}$ as a function of the only macroscopic source term $\langle \mathbf{v}_{\beta 0} \rangle^\beta$

$$\tilde{\mathbf{v}}_{\beta 0} = \mathbf{B} \cdot \langle \mathbf{v}_{\beta 0} \rangle^\beta \tag{A.3a}$$

$$\tilde{p}_{\beta 0} = \mathbf{b} \cdot \langle \mathbf{v}_{\beta 0} \rangle^\beta \tag{A.3b}$$

Here $\mathbf{B}$ and $\mathbf{b}$ are closure variable that are solution of the closure problem at order 0

$$\nabla \cdot \mathbf{B} = 0 \quad \text{in} \quad V_\beta \tag{A.4a}$$

$$0 = -\nabla \mathbf{b} + \nabla^2 \mathbf{B} + \varepsilon_\beta \mathbf{K}_\beta^{-1} \quad \text{in} \quad V_\beta \tag{A.4b}$$

$$\mathbf{B} = -\mathbf{I} \quad \text{on} \quad A_{\beta\sigma} \tag{A.4c}$$

$$\mathbf{B}\left(\mathbf{r} + \mathbf{l_i}\right) = \mathbf{B}\left(\mathbf{r}\right) \quad ; \quad \mathbf{b}\left(\mathbf{r} + \mathbf{l_i}\right) = \mathbf{b}\left(\mathbf{r}\right) \quad ; \quad i = 1, 2, 3 \tag{A.4d}$$

$$\langle \mathbf{B} \rangle^\beta = 0 \quad ; \quad \langle \mathbf{b} \rangle^\beta = 0 \tag{A.4e}$$

where the intrinsic permeability is defined as

$$\varepsilon_\beta \mathbf{K}_\beta^{-1} = -\frac{1}{V_\beta}\int_{A_{\beta\sigma}} \mathbf{n}_{\beta\sigma}\cdot\left(-\mathbf{I}\mathbf{b}+\nabla\mathbf{B}\right)dA \tag{A.5}$$

Similarly to the closure problem (14), the above system can easily be written in the form of an incompressible Stokes flow with no-slip boundary conditions using the following change of variable [58]: $\mathbf{B}' = \varepsilon_\beta^{-1}\left(\mathbf{B}+\mathbf{I}\right)\cdot\mathbf{K}_\beta$ and $\mathbf{b}' = \varepsilon_\beta^{-1}\mathbf{b}\cdot\mathbf{K}_\beta$

The solution of the closure problem at order 0 on a unit cell gives the value of the intrinsic permeability tensor $\mathbf{K}_\beta$. Moreover, the values of the closure variables $\mathbf{B}$ and $\mathbf{b}$ will be needed to solve the linearized closure problems at higher order. These properties is linked to the linearization method and motivates the need to solve the closure problems in a recursive way in order to linearized the results for high orders of the Reynolds number.

Order k = 1

Identifying the terms in Re^1 in the power-series decomposition of the deviation problem, one gets the linearized spatial deviation problem at order 1

$$\nabla\cdot\tilde{\mathbf{v}}_{\beta 1} = 0 \quad \text{in} \quad V_\beta \tag{A.6a}$$

$$\mathbf{v}_{\beta 0}\cdot\nabla\tilde{\mathbf{v}}_{\beta 0} = -\nabla\tilde{p}_{\beta 1} + \nabla^2\tilde{\mathbf{v}}_{\beta 1} - \frac{1}{V_\beta}\int_{A_{\beta\sigma}}\mathbf{n}_{\beta\sigma}\cdot\left(-\mathbf{I}\tilde{p}_{\beta 1}+\nabla\tilde{\mathbf{v}}_{\beta 1}\right)dA \quad \text{in} \quad V_\beta \tag{A.6b}$$

$$\tilde{\mathbf{v}}_{\beta 1} = -\langle\mathbf{v}_{\beta 1}\rangle^\beta \quad \text{on} \quad A_{\beta\sigma} \tag{A.6c}$$

$$\tilde{\mathbf{v}}_{\beta 1}\left(\mathbf{r}+\mathbf{e_i}\right) = \tilde{\mathbf{v}}_{\beta 1}\left(\mathbf{r}\right) \quad ; \quad \tilde{p}_{\beta 1}\left(\mathbf{r}+\mathbf{e_i}\right) = \tilde{p}_{\beta 1}\left(\mathbf{r}\right) \quad ; \quad i=1,2,3 \tag{A.6d}$$

$$\langle\tilde{\mathbf{v}}_{\beta 1}\rangle^\beta = 0 \quad ; \quad \langle\tilde{p}_{\beta 1}\rangle^\beta = 0 \tag{A.6e}$$

Note that the term $\mathbf{v}_{\beta 0}\cdot\nabla\tilde{\mathbf{v}}_{\beta 0}$ is at order 0. Thanks to the spacial decomposition of the velocity and (A.3a), it can be expressed using the zero order closure variables as

$$\begin{aligned}\mathbf{v}_{\beta 0}\cdot\nabla\tilde{\mathbf{v}}_{\beta 0} &= \left[\left(\mathbf{B}+\mathbf{I}\right)\cdot\langle\mathbf{v}_{\beta 0}\rangle^\beta\right]\cdot\left(\nabla\mathbf{B}\cdot\langle\mathbf{v}_{\beta 0}\rangle^\beta\right)\\ &= \left[\left(\nabla\mathbf{B}\right)^{T_{(123)}}\cdot\left(\mathbf{B}+\mathbf{I}\right)\right] : \langle\mathbf{v}_{\beta 0}\rangle^\beta\langle\mathbf{v}_{\beta 0}\rangle^\beta\end{aligned}$$

where the transpose operator is defined as $\mathcal{A}^{T_{(123)}} = \left(\mathcal{A}_{ijk}\mathbf{e}_i\mathbf{e}_j\mathbf{e}_k\right)^{T_{(123)}} = \mathcal{A}_{kij}\mathbf{e}_i\mathbf{e}_j\mathbf{e}_k$ for a third order tensor $\mathcal{A}$. Using this expression, the spatial deviation problem can be written in a more explicit form that exhibits different macroscopic source terms

$$\nabla\cdot\tilde{\mathbf{v}}_{\beta 1} = 0 \quad \text{in} \quad V_\beta \tag{A.7a}$$

$$\begin{aligned}&\left[\left(\nabla\mathbf{B}\right)^{T_{(123)}}\cdot\left(\mathbf{B}+\mathbf{I}\right)\right] : \langle\mathbf{v}_{\beta 0}\rangle^\beta\langle\mathbf{v}_{\beta 0}\rangle^\beta\\ &\qquad = -\nabla\tilde{p}_{\beta 1} + \nabla^2\tilde{\mathbf{v}}_{\beta 1} - \frac{1}{V_\beta}\int_{A_{\beta\sigma}}\mathbf{n}_{\beta\sigma}\cdot\left(-\mathbf{I}\tilde{p}_{\beta 1}+\nabla\tilde{\mathbf{v}}_{\beta 1}\right)dA \quad \text{in} \quad V_\beta\end{aligned} \tag{A.7b}$$

$$\tilde{\mathbf{v}}_{\beta 1} = -\langle\mathbf{v}_{\beta 1}\rangle^\beta \quad \text{on} \quad A_{\beta\sigma} \tag{A.7c}$$

$$\tilde{\mathbf{v}}_{\beta 1}\left(\mathbf{r}+\mathbf{l_i}\right) = \tilde{\mathbf{v}}_{\beta 1}\left(\mathbf{r}\right) \quad ; \quad \tilde{p}_{\beta 1}\left(\mathbf{r}+\mathbf{l_i}\right) = \tilde{p}_{\beta 1}\left(\mathbf{r}\right) \quad ; \quad i=1,2,3 \tag{A.7d}$$

$$\langle \tilde{\mathbf{v}}_{\beta 1} \rangle^{\beta} = 0 \quad ; \quad \langle \tilde{p}_{\beta 1} \rangle^{\beta} = 0 \tag{A.7e}$$

This last problem is linear and self-consistent because the closure variables $\mathbf{B}$ and $\mathbf{b}$ have been solved previously at order 0. Moreover, two macroscopic source terms are identified. The first one $\langle \mathbf{v}_{\beta 1} \rangle^{\beta}$ appears in the boundary condition and is very similar to the macroscopic source term at order 0. The second one $\langle \mathbf{v}_{\beta 0} \rangle^{\beta} \langle \mathbf{v}_{\beta 0} \rangle^{\beta}$ is new and arises in the momentum balance equation at order 1 due to the coupling between order 0 and 1. Using the superposition principle, the spatial deviations $\tilde{\mathbf{v}}_{\beta 1}$ and $\tilde{p}_{\beta 1}$ can be mapped using the macroscopic source terms

$$\tilde{\mathbf{v}}_{\beta 1} = \mathbf{B} \cdot \langle \mathbf{v}_{\beta 1} \rangle^{\beta} + \mathcal{C} : \langle \mathbf{v}_{\beta 0} \rangle^{\beta} \langle \mathbf{v}_{\beta 0} \rangle^{\beta} \tag{A.8a}$$

$$\tilde{p}_{\beta 1} = \mathbf{b} \cdot \langle \mathbf{v}_{\beta 1} \rangle^{\beta} + \mathbf{C} : \langle \mathbf{v}_{\beta 0} \rangle^{\beta} \langle \mathbf{v}_{\beta 0} \rangle^{\beta} \tag{A.8b}$$

where $\mathbf{B}$ and $\mathbf{b}$ are the closure variables that solve the same closure problem as previously introduced at order 0, and $\mathcal{C}$ and $\mathbf{C}$ are two new closure variables introduced for the second source term. They verify the following closure problem at order 1

$$\nabla \cdot \mathcal{C} = 0 \quad \text{in} \quad V_{\beta} \tag{A.9a}$$

$$\left[(\nabla \mathbf{B})^{T_{(123)}} \cdot (\mathbf{B} + \mathbf{I}) \right] = -\nabla \mathbf{C} + \nabla^2 \mathcal{C} - \frac{1}{V_{\beta}} \int_{A_{\beta\sigma}} \mathbf{n}_{\beta\sigma} \cdot (-\mathbf{I}\mathcal{C} + \nabla \mathcal{C}) \, dA \quad \text{in} \quad V_{\beta} \tag{A.9b}$$

$$\mathcal{C} = 0 \quad \text{on} \quad A_{\beta\sigma} \tag{A.9c}$$

$$\mathcal{C}(\mathbf{r} + \mathbf{l_i}) = \mathcal{C}(\mathbf{r}) \quad ; \quad \mathbf{C}(\mathbf{r} + \mathbf{l_i}) = \mathbf{C}(\mathbf{r}) \quad ; \quad i = 1, 2, 3 \tag{A.9d}$$

$$\langle \mathcal{C} \rangle^{\beta} = 0 \quad ; \quad \langle \mathbf{C} \rangle^{\beta} = 0 \tag{A.9e}$$

The solution of this problem only depends on the geometry of the unit cell, and not on the Reynolds number nor the macroscopic pressure gradient orientation. Once again, to deal with the integro-differential nature of this problem, it is convenient to define

$$\varepsilon_{\beta} \mathbf{K}_{\beta}^{-1} \cdot \mathcal{H}_{\beta} = -\frac{1}{V_{\beta}} \int_{A_{\beta\sigma}} \mathbf{n}_{\beta\sigma} \cdot (-\mathbf{I}\mathcal{C} + \nabla \mathcal{C}) \, dA \tag{A.10}$$

where $\mathcal{H}_{\beta}$ can be interpreted as a correction to the intrinsic permeability to account for inertial effects contributing to the global permeability tensor $\mathbf{H}_{\beta}$ at order 1. The surface integral being constant within a given unit cell, $\varepsilon_{\beta} \mathbf{K}_{\beta}^{-1} \cdot \mathcal{H}_{\beta}$ can be seen as a constant source term. This suggests to proceed once more to a change of variable

$$\mathcal{C} = \mathcal{C}' + \mathscr{S} : \varepsilon_{\beta} \mathbf{K}_{\beta}^{-1} \cdot \mathcal{H}_{\beta} \quad ; \quad \mathbf{C} = \mathbf{C}' + \mathcal{S} : \varepsilon_{\beta} \mathbf{K}_{\beta}^{-1} \cdot \mathcal{H}_{\beta} \tag{A.11}$$

so that the integro-differential closure problem can be decomposed into two purely differential problems

$$\nabla \cdot \mathcal{C}' = 0 \quad \text{in} \quad V_{\beta} \tag{A.12a}$$

$$\left[(\nabla \mathbf{B})^{T_{(123)}} \cdot (\mathbf{B} + \mathbf{I}) \right] = -\nabla \mathbf{C}' + \nabla^2 \mathcal{C}' \quad \text{in} \quad V_{\beta} \tag{A.12b}$$

$$\mathcal{C}' = 0 \quad \text{on} \quad A_{\beta\sigma} \tag{A.12c}$$

$$\mathcal{C}'(\mathbf{r}+\mathbf{l_i}) = \mathcal{C}'(\mathbf{r}) \quad ; \quad \mathbf{C}'(\mathbf{r}+\mathbf{l_i}) = \mathbf{C}'(\mathbf{r}) \quad ; \quad i = 1,2,3 \tag{A.12d}$$

$$\langle \mathbf{C}' \rangle^\beta = 0 \tag{A.12e}$$

and

$$\nabla \cdot \mathscr{S} = 0 \quad \text{in} \quad V_\beta \tag{A.13a}$$

$$0 = -\nabla \mathcal{S} + \nabla^2 \mathscr{S} + \mathscr{I} \quad \text{in} \quad V_\beta \tag{A.13b}$$

$$\mathscr{S} = 0 \quad \text{on} \quad A_{\beta\sigma} \tag{A.13c}$$

$$\mathscr{S}(\mathbf{r}+\mathbf{l_i}) = \mathscr{S}(\mathbf{r}) \quad ; \quad \mathcal{S}(\mathbf{r}+\mathbf{l_i}) = \mathcal{S}(\mathbf{r}) \quad ; \quad i = 1,2,3 \tag{A.13d}$$

$$\langle \mathcal{S} \rangle^\beta = 0 \tag{A.13e}$$

Problem (A.13) is very similar to the practical form of the Stokes closure problem but needs to be solved for a fourth order tensor $\mathscr{S}$ and a source term $\mathscr{I} = \delta_{il}\delta_{jk}\mathbf{e}_i\mathbf{e}_j\mathbf{e}_k\mathbf{e}_l$.

The superficial averages of the closure variables $\mathcal{C}$ being null, one gets

$$0 = \langle \mathcal{C} \rangle^\beta = \langle \mathcal{C}' \rangle^\beta + \langle \mathscr{S} \rangle^\beta : \varepsilon_\beta \mathbf{K}_\beta^{-1} \cdot \mathcal{H}_\beta \tag{A.14}$$

so that

$$\varepsilon_\beta \mathbf{K}_\beta^{-1} \cdot \mathcal{H}_\beta = -\left(\langle \mathscr{S} \rangle^\beta \right)^{-1} : \langle \mathcal{C}' \rangle^\beta \tag{A.15}$$

After making use of some tensor algebra and the properties of problem (A.13), the following expression for the correction tensor at order 0 is obtained

$$\mathcal{H}_\beta = -\langle \mathcal{C}' \rangle^\beta \tag{A.16}$$

Order k = 2

Applying the same pocedure as above, coefficients in Re^2 are identified in the expanded closure problem, giving the deviation problem at order 2

$$\nabla \cdot \tilde{\mathbf{v}}_{\beta 2} = 0 \quad \text{in} \quad V_\beta \tag{A.17a}$$

$$\mathbf{v}_{\beta 0} \cdot \nabla \tilde{\mathbf{v}}_{\beta 1} + \mathbf{v}_{\beta 1} \cdot \nabla \tilde{\mathbf{v}}_{\beta 0} = -\nabla \tilde{p}_{\beta 2} + \nabla^2 \tilde{\mathbf{v}}_{\beta 2} - \frac{1}{V_\beta} \int_{A_{\beta\sigma}} \mathbf{n}_{\beta\sigma} \cdot \left(-\mathbf{I}\tilde{p}_{\beta 2} + \nabla \tilde{\mathbf{v}}_{\beta 2} \right) dA \tag{A.17b}$$

$$\tilde{\mathbf{v}}_{\beta 2} = -\langle \mathbf{v}_{\beta 2} \rangle^\beta \quad \text{on} \quad A_{\beta\sigma} \tag{A.17c}$$

$$\tilde{\mathbf{v}}_{\beta 2}(\mathbf{r}+\mathbf{e_i}) = \tilde{\mathbf{v}}_{\beta 2}(\mathbf{r}) \quad ; \quad \tilde{p}_{\beta 2}(\mathbf{r}+\mathbf{e_i}) = \tilde{p}_{\beta 2}(\mathbf{r}) \quad ; \quad i = 1,2,3 \tag{A.17d}$$

$$\langle \tilde{\mathbf{v}}_{\beta 2} \rangle^\beta = 0 \quad ; \quad \langle \tilde{p}_{\beta 2} \rangle^\beta = 0 \tag{A.17e}$$

Once again the non-linear terms only involve variables at lower orders. After some rearrangements, the problem can be expressed in a more explicit form that exhibits all the different macroscopic source terms

$$\nabla \cdot \tilde{\mathbf{v}}_{\beta 2} = 0 \quad \text{in} \quad V_\beta \tag{A.18a}$$

$$\Big[(\nabla\mathbf{B})^{T_{(123)}}\cdot(\mathbf{B}+\mathbf{I})\Big]:\Big[\langle\mathbf{v}_{\beta 0}\rangle^{\beta}\langle\mathbf{v}_{\beta 1}\rangle^{\beta}+\langle\mathbf{v}_{\beta 1}\rangle^{\beta}\langle\mathbf{v}_{\beta 0}\rangle^{\beta}\Big]$$
$$+\Big[(\nabla\mathcal{C})^{T_{(1234)}}\cdot(\mathbf{B}+\mathbf{I})+(\nabla\mathbf{B})^{T_{(123)}}\cdot\mathcal{C}\Big]\vdots\langle\mathbf{v}_{\beta 0}\rangle^{\beta}\langle\mathbf{v}_{\beta 0}\rangle^{\beta}\langle\mathbf{v}_{\beta 0}\rangle^{\beta} \tag{A.18b}$$
$$=-\nabla\tilde{p}_{\beta 2}+\nabla^2\tilde{\mathbf{v}}_{\beta 2}-\frac{1}{V_\beta}\int_{A_{\beta\sigma}}\mathbf{n}_{\beta\sigma}\cdot(-\mathbf{I}\tilde{p}_{\beta 2}+\nabla\tilde{\mathbf{v}}_{\beta 2})\,dA\quad\text{in}\quad V_\beta$$

$$\tilde{\mathbf{v}}_{\beta 2}=-\langle\mathbf{v}_{\beta 2}\rangle^{\beta}\quad\text{on}\quad A_{\beta\sigma} \tag{A.18c}$$

$$\tilde{\mathbf{v}}_{\beta 2}(\mathbf{r}+\mathbf{l_i})=\tilde{\mathbf{v}}_{\beta 2}(\mathbf{r})\quad;\quad\tilde{p}_{\beta 2}(\mathbf{r}+\mathbf{l_i})=\tilde{p}_{\beta 2}(\mathbf{r})\quad;\quad i=1,2,3 \tag{A.18d}$$

$$\langle\tilde{\mathbf{v}}_{\beta 2}\rangle^{\beta}=0\quad;\quad\langle\tilde{p}_{\beta 2}\rangle^{\beta}=0 \tag{A.18e}$$

where the notation $\mathscr{A}^{T_{(1234)}}=(\mathscr{A}_{ijkl}\mathbf{e}_i\mathbf{e}_j\mathbf{e}_k\mathbf{e}_l)^{T_{(1234)}}=\mathscr{A}_{lijk}\mathbf{e}_i\mathbf{e}_j\mathbf{e}_k\mathbf{e}_l$ has been used for the transpose of a fourth order tensor $\mathscr{A}$. In this problem, three independent source terms are identified. The first one $\langle\mathbf{v}_{\beta 2}\rangle^{\beta}$ appears in the boundary condition at $A_{\beta\sigma}$ just as in the case of order 0 and 1. The second one $\big[\langle\mathbf{v}_{\beta 0}\rangle^{\beta}\langle\mathbf{v}_{\beta 1}\rangle^{\beta}+\langle\mathbf{v}_{\beta 1}\rangle^{\beta}\langle\mathbf{v}_{\beta 0}\rangle^{\beta}\big]$ is similar to the second source term of order 1. The third one $\langle\mathbf{v}_{\beta 0}\rangle^{\beta}\langle\mathbf{v}_{\beta 0}\rangle^{\beta}\langle\mathbf{v}_{\beta 0}\rangle^{\beta}$ is a new source term that appears in the momentum balance equation. This terms couple order 0 and 1 with the solution of the linearized deviations at order 2. Based on these observations, the following decomposition is introduced

$$\tilde{\mathbf{v}}_{\beta 2}=\mathbf{B}\cdot\langle\mathbf{v}_{\beta 2}\rangle^{\beta}+\mathcal{C}:\Big(\langle\mathbf{v}_{\beta 0}\rangle^{\beta}\langle\mathbf{v}_{\beta 1}\rangle^{\beta}+\langle\mathbf{v}_{\beta 1}\rangle^{\beta}\langle\mathbf{v}_{\beta 0}\rangle^{\beta}\Big)+\mathscr{E}\vdots\langle\mathbf{v}_{\beta 0}\rangle^{\beta}\langle\mathbf{v}_{\beta 0}\rangle^{\beta}\langle\mathbf{v}_{\beta 0}\rangle^{\beta} \tag{A.19a}$$

$$\tilde{p}_{\beta 2}=\mathbf{b}\cdot\langle\mathbf{v}_{\beta 2}\rangle^{\beta}+\mathbf{C}:\Big(\langle\mathbf{v}_{\beta 0}\rangle^{\beta}\langle\mathbf{v}_{\beta 1}\rangle^{\beta}+\langle\mathbf{v}_{\beta 1}\rangle^{\beta}\langle\mathbf{v}_{\beta 0}\rangle^{\beta}\Big)+\mathcal{E}\vdots\langle\mathbf{v}_{\beta 0}\rangle^{\beta}\langle\mathbf{v}_{\beta 0}\rangle^{\beta}\langle\mathbf{v}_{\beta 0}\rangle^{\beta} \tag{A.19b}$$

where $\mathbf{B}$, $\mathbf{b}$ and $\mathcal{C}$ and $\mathbf{C}$ are the closure variables at order 0 and order 1 respectively. The new closure variables $\mathscr{E}$ and $\mathcal{E}$ verify the following closure problem

$$\nabla\cdot\mathscr{E}=0\quad\text{in}\quad V_\beta \tag{A.20a}$$

$$\Big[(\nabla\mathcal{C})^{T_{(1234)}}\cdot(\mathbf{B}+\mathbf{I})+(\nabla\mathbf{B})^{T_{(123)}}\cdot\mathcal{C}\Big]=$$
$$-\nabla\mathcal{E}+\nabla^2\mathscr{E}-\frac{1}{V_\beta}\int_{A_{\beta\sigma}}\mathbf{n}_{\beta\sigma}\cdot(-\mathbf{I}\mathcal{E}+\nabla\mathscr{E})\,dA\quad\text{in}\quad V_\beta \tag{A.20b}$$

$$\mathscr{E}=0\quad\text{on}\quad A_{\beta\sigma} \tag{A.20c}$$

$$\mathscr{E}(\mathbf{r}+\mathbf{l_i})=\mathscr{E}(\mathbf{r})\quad;\quad\mathcal{E}(\mathbf{r}+\mathbf{l_i})=\mathcal{E}(\mathbf{r})\quad;\quad i=1,2,3 \tag{A.20d}$$

$$\langle\mathscr{E}\rangle^{\beta}=0\quad;\quad\langle\mathcal{E}\rangle^{\beta}=0 \tag{A.20e}$$

The integral term is defined as

$$\varepsilon_\beta\mathbf{K}_\beta^{-1}\cdot\mathscr{J}_\beta=-\frac{1}{V_\beta}\int_{A_{\beta\sigma}}\mathbf{n}_{\beta\sigma}\cdot(-\mathbf{I}\mathcal{E}+\nabla\mathscr{E})\,dA \tag{A.21}$$

Once again, $\mathscr{J}_\beta$ can be interpreted as a correction tensor of the intrinsic permeability $\mathbf{H}_\beta$ at order 2.

To solve this integro-differential problem, the following decomposition is introduced based on the superposition principle

$$\mathscr{E}=\mathscr{E}'+\mathscr{T}:\varepsilon_\beta\mathbf{K}_\beta^{-1}\cdot\mathscr{J}_\beta \tag{A.22a}$$

$$\mathcal{E} = \mathcal{E}' + \mathcal{T} : \varepsilon_\beta \mathbf{K}_\beta^{-1} \cdot \mathscr{J}_\beta \tag{A.22b}$$

It follows that the closure problem can be decomposed into two purely differential closure problems

$$\nabla \cdot \mathscr{E}' = 0 \quad \text{in} \quad V_\beta \tag{A.23a}$$

$$\left[(\nabla \mathcal{C})^{T_{(1234)}} \cdot (\mathbf{B} + \mathbf{I}) + (\nabla \mathbf{B})^{T_{(123)}} \cdot \mathcal{C} \right] = -\nabla \mathcal{E}' + \nabla^2 \mathscr{E}' \quad \text{in} \quad V_\beta \tag{A.23b}$$

$$\mathscr{E}' = 0 \quad \text{on} \quad A_{\beta\sigma} \tag{A.23c}$$

$$\mathscr{E}'(\mathbf{r} + \mathbf{l_i}) = \mathscr{E}'(\mathbf{r}) \quad ; \quad \mathcal{E}'(\mathbf{r} + \mathbf{l_i}) = \mathcal{E}'(\mathbf{r}) \quad ; \quad i = 1, 2, 3 \tag{A.23d}$$

$$\langle \mathcal{E}' \rangle^\beta = 0 \tag{A.23e}$$

and

$$\nabla \cdot \mathscr{T} = 0 \quad \text{in} \quad V_\beta \tag{A.24a}$$

$$0 = -\nabla \mathcal{T} + \nabla^2 \mathscr{T} + \mathscr{I} \quad \text{in} \quad V_\beta \tag{A.24b}$$

$$\mathscr{T} = 0 \quad \text{on} \quad A_{\beta\sigma} \tag{A.24c}$$

$$\mathscr{T}(\mathbf{r} + \mathbf{l_i}) = \mathscr{T}(\mathbf{r}) \quad ; \quad \mathcal{T}(\mathbf{r} + \mathbf{l_i}) = \mathcal{T}(\mathbf{r}) \quad ; \quad i = 1, 2, 3 \tag{A.24d}$$

$$\langle \mathcal{T} \rangle^\beta = 0 \tag{A.24e}$$

Note that $\mathscr{T}$ is solution of the exact same closure problem as Eqs. (A.13), so that $\mathscr{T} = \mathscr{S}$.

To compute the correction tensor at order 2, a similar strategy as at order 1 is used. By definition of the intrinsic average (A.20e), one can write the equality

$$\begin{aligned} \langle \mathscr{E} \rangle^\beta = 0 &= \langle \mathscr{E}' \rangle^\beta + \langle \mathscr{T} \rangle^\beta : \varepsilon_\beta \mathbf{K}_\beta^{-1} \cdot \mathscr{J}_\beta \\ &= \langle \mathscr{E}' \rangle^\beta + \varepsilon_\beta^{-1} \mathbf{K}_\beta \cdot \varepsilon_\beta \mathbf{K}_\beta^{-1} \cdot \mathscr{J}_\beta \\ &= \langle \mathscr{E}' \rangle^\beta + \mathscr{J}_\beta \end{aligned} \tag{A.25}$$

so that the value of $\mathscr{J}_\beta$ is obtained from $\mathscr{J}_\beta = -\langle \mathscr{E}' \rangle^\beta$.

Total deviations

The total deviations $\tilde{\mathbf{v}}_\beta$ and $\tilde{p}_\beta$ can be reconstructed from Eq. (A.1) using the mappings (A.3), (A.8), and (A.19), giving up to order 2

$$\begin{aligned} \tilde{\mathbf{v}}_\beta &= \tilde{\mathbf{v}}_{\beta 0} + \tilde{\mathbf{v}}_{\beta 1} Re_p + \tilde{\mathbf{v}}_{\beta 2} Re_p^2 + ... \\ &= \mathbf{B} \cdot \left[\langle \mathbf{v}_{\beta 0} \rangle^\beta + Re_p \langle \mathbf{v}_{\beta 1} \rangle^\beta + Re_p^2 \langle \mathbf{v}_{\beta 2} \rangle^\beta + ... \right] \\ &\quad + \mathcal{C} : Re_p \left[\langle \mathbf{v}_{\beta 0} \rangle^\beta \langle \mathbf{v}_{\beta 0} \rangle^\beta + Re_p \left(\langle \mathbf{v}_{\beta 1} \rangle^\beta \langle \mathbf{v}_{\beta 0} \rangle^\beta + \langle \mathbf{v}_{\beta 0} \rangle^\beta \langle \mathbf{v}_{\beta 1} \rangle^\beta \right) + ... \right] \\ &\quad + \mathscr{E} \vdots Re_p^2 \left[\langle \mathbf{v}_{\beta 0} \rangle^\beta \langle \mathbf{v}_{\beta 0} \rangle^\beta \langle \mathbf{v}_{\beta 0} \rangle^\beta + ... \right] + ... \end{aligned} \tag{A.26}$$

and similarly for the pressure deviation. Higher order developments can show that the total deviations are recursively recovered. Therefore, it is possible to simply group all these terms to obtain a second order expansion of the total deviations with the total macroscopic source terms as follows

$$\tilde{\mathbf{v}}_\beta = \mathbf{B} \cdot \langle \mathbf{v}_\beta \rangle^\beta + \mathcal{C} : Re_p \langle \mathbf{v}_\beta \rangle^\beta \langle \mathbf{v}_\beta \rangle^\beta + \mathscr{E} \vdots Re_p^2 \langle \mathbf{v}_\beta \rangle^\beta \langle \mathbf{v}_\beta \rangle^\beta \langle \mathbf{v}_\beta \rangle^\beta + ... \tag{A.27a}$$

$$\tilde{p}_\beta = \mathbf{b} \cdot \langle \mathbf{v}_\beta \rangle^\beta + \mathbf{C} : Re_p \langle \mathbf{v}_\beta \rangle^\beta \langle \mathbf{v}_\beta \rangle^\beta + \mathcal{E} \vdots Re_p^2 \langle \mathbf{v}_\beta \rangle^\beta \langle \mathbf{v}_\beta \rangle^\beta \langle \mathbf{v}_\beta \rangle^\beta + ... \tag{A.27b}$$

Similarly to the non-linear case, it is possible to close the averaged equation (6b) by introducing the above linearized mapping of the spatial deviations and identifying the corrective effective tensors at each order. Identical closed averaged equations are obtained but the effective parameters are linearized around the Reynolds number. Up to order 2, the linearized global permeability tensor is

$$\mathbf{H}_\beta^{-1} = \mathbf{K}_\beta^{-1} \cdot \Big(\mathbf{I} + Re_p \mathcal{H}_\beta \cdot \langle \mathbf{v}_\beta \rangle^\beta + Re_p^2 \mathscr{J}_\beta : \langle \mathbf{v}_\beta \rangle^\beta \langle \mathbf{v}_\beta \rangle^\beta + ... \Big) \tag{A.28}$$

where the Forchheimer correction tensor can be directly identified as

$$\mathbf{F}_\beta = Re_p \mathcal{H}_\beta \cdot \langle \mathbf{v}_\beta \rangle^\beta + Re_p^2 \mathscr{J}_\beta : \langle \mathbf{v}_\beta \rangle^\beta \langle \mathbf{v}_\beta \rangle^\beta + ... \tag{A.29}$$

B Comparison of computation times of the closure problems

Here the computational costs of solving the linearized and non-linear closure problems are compared in the weak inertia regime where the linearized closure problem is valid ($Re_k \lesssim 1$). In two dimensions, the general non-linear closure requires to solve one non-linear vectorial problem (Eqs. (17)), plus $2^{2-1} = 2$ linear vector problems (Eqs. (16)) over a unit cell *for each value of the pore Reynolds number Re_p and the macroscopic pressure gradient orientation θ*. On the other hand, the linearized closure truncated at order 2 in Reynolds number introduces 3 linear tensor closure problems of increasing orders: at order 0 a second-order tensor problem (Eqs. (A.4)), at order 1 a third-order tensor problem (Eqs. (A.9)), and at order 2 a fourth-order tensor problem (Eqs. (A.20)). In total, in two dimensions, the numerical resolution of the linearized closure up to order 2 consists of solving $2^{2-1} + 2^{3-1} + 2^{4-1} = 14$ vector problems with Stokes-like structure over the same unit cell but without any dependency on the local macroscopic flow.

Computation times for numerical simulations of the non-linear and linearized closure problems up to order 2 were compared on the symmetric unit cell presented in Fig. 2a. The same mesh composed of 230,000 elements was used for all the simulations in order to ensure mesh independence on the numerical results, limit the propagation of numerical errors through the incremental linearized methodology and measure computation times for comparable numerical resources. Computations were performed in Comsol Multiphysics as described in the main text.

Numerical simulations of the general non-linear closure problem take approximately 200 seconds for each value of pore Reynolds numbers Re_p and macroscopic pressure gradient orientation θ. In contrast, solving the 14 vector problems of the linearized closure truncated at order 2 take approximately 1800 seconds. However these are valid for any (Re_p, θ) within the domain of validity of the linear problem. Therefore solving the linearized closure problem truncated at order 2 costs as much as solving the non-linear problem for 1880s/200s = 9 values of the couples of parameter (Re_p, θ).

The use of the linearized closure problem is interesting when more than 10 points are needed for the tabulation of the Forchheimer correction tensor. For instance, the results presented in Fig. 3 for a unit cell with solid square obstacle and porosity $\varepsilon_\beta = 0.75$ required approximately 50 computations of the non-linear closure problem with different values of (Re_p, θ) satisfying $Re_k < 0.1$, thus making the linearized closure much more cost efficient in this special case.